The Astrophysical Journal, 940:76 (28pp), 2022 November 20 https://doi.org/10.3847/1538-4357/ac94c5

Blanco DECam Bulge Survey (BDBS). VII. Multiple Populations in Globular Clusters of the Galactic Bulge

Justin A. Kader[1,2], Catherine A. Pilachowski[2], Christian I. Johnson[2,3], R. Michael Rich[4], Michael D. Young[5], Iulia T. Simion[6], William I. Clarkson[7], Scott Michael[2], Andrea Kunder[8], Anna Katherina Vivas[9], Andreas J. Koch-Hansen[10], and Tommaso Marchetti[11]

[1] Department of Physics and Astronomy, 4129 Frederick Reines Hall, University of California, Irvine, CA 92697, USA; kaderj@uci.edu
[2] Department of Astronomy, Indiana University, SW319, 727 East 3rd Street, Bloomington, IN 47405-7105, USA
[3] Space Telescope Science Institute, 3700 San Martin Drive, Baltimore, MD 21218, USA
[4] Department of Physics and Astronomy, UCLA, 430 Portola Plaza, Box 951547, Los Angeles, CA 90095-1547, USA
[5] Indiana University, University Information Technology Services, CIB 2709 East 10th Street, Bloomington, IN 47401, USA
[6] Key Laboratory for Research in Galaxies and Cosmology, Shanghai University, 80 Nandan Road, Shanghai 200030, People's Republic of China
[7] Department of Natural Sciences, University of Michigan-Dearborn, 4901 Evergreen Road, Dearborn, MI 48128, USA
[8] Department of Natural Sciences, Saint Martin's University, 5000 Abbey Way SE, Lacey, WA 98503, USA
[9] Cerro Tololo Inter-American Observatory, NSF's National Optical-Infrared Astronomy Research Laboratory, Casilla 603, La Serena, Chile
[10] Zentrum für Astronomie der Universität Heidelberg, Astronomisches Rechen-Institut, Mönchhofstraße 12, D69120, D-69120, Heidelberg, Germany
[11] European Southern Observatory, Karl-Schwartzschild-Straße 2, 85748D-85748 Garching bei München, Germany
Received 2022 May 31; revised 2022 September 20; accepted 2022 September 22; published 2022 November 22

Abstract

We present photometric evidence for multiple stellar populations (MPs) in 14 globular clusters (GCs) toward the southern Galactic bulge. The photometric data come as part of the Blanco DECam Bulge Survey, which is a deep, wide-field near-UV-near-IR (*ugriz*Y) survey of the southern Galactic bulge. Here, we present the first systematic study of bulge GC multiple populations with deep photometry including the *u* band, which is a crucial indicator of the abundance of CNO-bearing molecules in stellar atmospheres. We identify cluster members using Gaia EDR3 proper motion measurements, and then isolate red giant branch stars using r versus $u-r$ color–magnitude diagrams. We find evidence suggesting all 14 clusters host at least two populations, and NGC 6441, NGC 6626, and NGC 6656 appear to have at least three populations. Many of these clusters are not part of the Hubble Space Telescope (HST) surveys nor do they have comprehensive spectroscopic analyses so we are presenting the first evidence of MPs in several clusters. Not only do we find a strong anticorrelation between the fraction of first-generation stars and cluster absolute V magnitude, but the correlation coefficient and cluster-to-cluster scatter are similar to the results obtained from HST. Our ground-based data extend to much larger radial distances than similar HST observations, enabling a reliable estimate of the global fraction of first-generation stars in each cluster. This study demonstrates that ground-based *u*-band photometry as provided by DECam will prove powerful in the study of multiple populations in resolved GCs.

Unified Astronomy Thesaurus concepts: Globular star clusters (656); Red giant stars (1372); Broad band photometry (184); Galactic bulge (2041); Ultraviolet astronomy (1736)

1. Introduction

The phenomenon of multiple stellar populations (MPs) in globular clusters (GCs) has become an area of intense scrutiny during the last 20 yr. Photometric and spectroscopic studies have found most Galactic GCs are host to MPs (Gratton et al. 2012; Bastian & Lardo 2018; Gratton et al. 2019). MPs have also been found in extragalactic GCs, e.g., in the Large Magellanic Cloud (Mucciarelli et al. 2008, 2009, 2010; Piatti & Koch 2018), the Small Magellanic Cloud (Hollyhead et al. 2017), Sagittarius dSph (Carretta et al. 2014; Boberg et al. 2015; Sbordone et al. 2015), Fornax dSph (Letarte et al. 2006), M31 (Schiavon et al. 2013; Colucci et al. 2014; Sakari et al. 2015), WLM (Larsen et al. 2014), and see Section 2.1.5 of Bastian & Lardo (2018). The idea that a multiply-populated GC is a *normal* GC is supported by a wealth of both spectroscopic and photometric evidence. Chemical abundance studies of individual clusters starting many decades ago began to demonstrate light element abundance inhomogeneities among red giant, horizontal branch, and even main-sequence (MS) stars (e.g., Popper 1947; Harding 1962; Cohen 1978) and modern studies have continued to reveal star-to-star abundance variations in an ever-growing number of GCs (see, e.g., references in the reviews by Gratton et al. 2012; Bastian & Lardo 2018; Gratton et al. 2019). Recent large-scale photometric studies have revealed color broadening and even splits in the giant branches and MSs of clusters, particularly when blue or ultraviolet (UV) filters are utilized (Piotto 2008; Lardo et al. 2011; Monelli et al. 2013; Lee 2015; Piotto et al. 2015; Milone et al. 2017; Bonatto et al. 2019; Hartmann et al. 2022). These color spreads are well correlated with the light element spreads found in spectroscopic studies (Marino et al. 2008; Carretta et al. 2009). The MPs found in MS stars suggest that the abundance variations are primordial, and not the result of self-enrichment via mixing processes in evolved stars (Gratton et al. 2001; Gerber et al. 2019). The commonly adopted picture is that the first generation (1G) of stars formed with chemical abundances similar to field stars at the same metallicity and subsequently polluted the intracluster environment, giving rise to a second generation (2G) at the same metallicity but enriched

in proton-capture reaction products of the CNO, NeNa, and MgAl chains (Carretta et al. 2010a). The precise nature of the polluting stars from the first-generation (e.g., massive asymptotic giant branch (AGB) stars, fast rotating massive stars or binaries, supermassive stars, etc.) remains an open question (Renzini 2008; Valcarce & Catelan 2011; Gratton et al. 2012; Bastian & Lardo 2018; Gratton et al. 2019; Vesperini et al. 2021). Whether this picture also applies to Galactic bulge GCs is unclear since the role of cluster environment and cluster global properties in the MP phenomenon has yet to be understood (Carretta 2019).

The presence and complexity of the MP phenomenon in inner Galaxy GCs is of key importance to the question of bulge formation (Tang et al. 2017; Schiavon et al. 2017a; Muñoz et al. 2020). The presence of a large population of inner Galaxy field stars with abundance patterns similar to those of 2G stars suggests that the destruction of an early precursor population of GCs may have contributed to the assembly of the Galactic bulge and the early Galaxy (Schiavon et al. 2017b; Tang et al. 2020), but more work regarding MPs in bulge GCs is needed in order to evaluate this hypothesis. One relevant connection is the discovery of MPs with different ages and metallicities in the massive GC-like object Terzan 5, which has led to speculation that it is the nucleus of a disrupted dwarf galaxy and a relic of the bulge coalescence process (Ferraro et al. 2009, 2021; Origlia et al. 2013; Massari et al. 2014), and recent observations of the inner bulge cluster Liller 1 indicate that it has similar properties to Terzan 5 (Saracino et al. 2015). Although there are several important studies of MPs in inner Galaxy GCs (Salinas & Strader 2015; Bica et al. 2016; Dias et al. 2016; Kerber et al. 2018; Carretta 2019; Geisler et al. 2021), these systems remain understudied compared to their halo and disk counterparts. A better understanding of inner Galaxy GCs is needed for a comprehensive view of the Galactic bulge.

We have initiated a program to specifically study the phenomenon of MPs in the GCs of the inner Galaxy using photometry from the Blanco DECam Bulge Survey (BDBS) (Johnson et al. 2020; Rich et al. 2020). These clusters traditionally are difficult to study, owing to the crowded fields they inhabit and to the strong extinction and differential reddening of their light along the lines of sight. The aims of this program are twofold; to broaden the picture of MPs in GCs by including many of the old, metal-rich GCs that exist in the Galactic bulge (Bica et al. 2016; Baumgardt et al. 2020), and to demonstrate the efficacy of ground-based photometric data in finding MPs when cluster membership and reddening are carefully considered. The BDBS field contains 26 known Galactic GCs (Johnson et al. 2020; Rich et al. 2020), and enables the identification and characterization of MPs in these clusters using the high-resolution, dereddened six-band *ugrizY* photometric point-source catalog that reaches down to at least the bottom of the red giant branch (RGB) of the GCs.

The $u-g$ color index is correlated with the observed light element (e.g., Na, N) abundances, such that N-rich/C-poor stars are redder in $u-g$, similar to the way in which the $U-B$ index is sensitive to light element variations (Marino et al. 2008; Yong et al. 2008; Lardo et al. 2011; Sbordone et al. 2011; Monelli et al. 2013; Lee 2019; Lim et al. 2021). Conversely, N-poor (Na-poor; 1G) stars appear red in $g-i$, similar to the $B-I$ index, since the same CN molecular bands fall within these particular Sloan and Johnson filters (Sbordone et al. 2011; Monelli et al. 2013). CNO abundance variations can be detected using blue and near-UV (NUV) filters because various strong molecular absorption bands (OH, CN, NH, CH) are found blueward of ∼4000 Å in giant atmospheres (Sbordone et al. 2011; Piotto et al. 2015). The pseudo-color index $(u-g)-(g-i)$, commonly referred to as C_{ugi}, is a beneficial indicator for separating stars of varying light element abundances (Bono et al. 2018).

In this paper, we analyze high-quality, dereddened photometric data to identify and characterize MPs in the 14 most massive GCs residing in the BDBS footprint. The paper is organized as follows. In Section 2, we briefly review the BDBS observations and basic data reduction, the methods used to remove contaminant noncluster stars and correct the photometry for differential reddening, and we introduce the GC sample. In Section 3, we describe the method used to identify and characterize MPs on the RGBs of each target cluster. The resulting population ratios and univariate correlations with global cluster parameters are presented in Section 4. In Section 5, we interpret our results in the context of GC evolution. A summary of the work, and our conclusions, can be found in Section 6.

2. Observations and Data

In this section, we briefly discuss the BDBS point-source catalog, photometric calibrations, and reddening corrections. We focus mainly on the methods used to eliminate contaminant noncluster stars from the data set, and the method employed to isolate red giant stars for each cluster. A fully detailed explanation of the image processing, photometric calibration, and construction of the BDBS catalog can be found in Johnson et al. (2020). A more complete description of the BDBS project history, motivation, instrumentation, and goals can be found in Rich et al. (2020). A full presentation of the methods used to correct the photometry in the GC fields for differential reddening can be found in Kader et al. (2022).

2.1. BDBS Catalog

The Blanco Dark Energy Camera (DECam) Bulge Survey (BDBS; Rich et al. 2020; Johnson et al. 2020) is the first optical photometric survey of the southern Galactic bulge of its kind in terms of both its photometric baseline, depth, and areal coverage. Observations took place in 2013 June—July and 2014 July using the DECam imager, which is mounted on the CTIO Blanco 4 m telescope. The program observations covered 200 $\deg^2$ of the southern Galactic bulge in 90 unique DECam pointings, utilizing six NUV to near-infrared (NIR) (*ugrizY*) passbands reaching down to the bulge main-sequence turnoff (MSTO). Typical seeing in the u band was $0\farcs8$–$1\farcs2$. Nearly the entire BDBS field is contained within the 300 $\deg^2$ Vista Variables in Via Lactea (VVV; Minniti et al. 2010) NIR photometric survey of the Galactic bar and bulge, which was used to de-redden the BDBS photometry via construction of a high-resolution ($1'$) dust map (Simion et al. 2017). The resulting source catalog contains dereddened, point-spread function fit, six-band NUV-NIR photometry of 250 million unique point sources across 200 square degrees of the southern Galactic bulge (Johnson et al. 2020). Since the relevant spatial scales in this study of GCs are often smaller than $1'$, we generated our own extinction maps to correct for differential reddening on finer angular scales (down to $5''$). These maps are described in (J. A. Kader et al. 2022, submitted). Reddening-corrected photometric colors and apparent magnitudes are indicated with

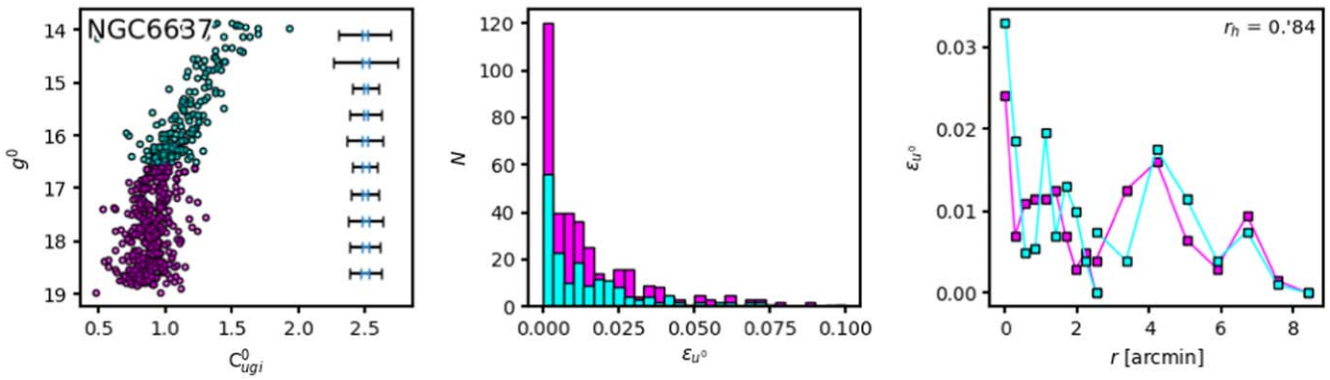

Figure 1. Photometric errors in the u band are shown for the bright and faint portions of the RGB of NGC 6637. The CMD in the left panel shows cluster member red giants, and the error bars show the mean photometric error in C_{ugi} as a function of g magnitude (blue bars) and the 1σ dispersion in C_{ugi} colors per bin (black bars). The u-band photometric measurement errors are small ($\lesssim$0.05 mag) and do not vary appreciably along the RGB, provided the faintest RGB stars are above $\sim$20 mag in u. This is illustrated in the center panel, which shows that the distributions over ε_u for the bright and faint RGB stars overlap significantly. It can be seen that the distribution of ε_u for the faint RGB stars has a slightly longer tail toward larger errors. The right panel shows the radial distributions in median u-band photometric error, for the bright and faint RGB stars. Beyond $\sim$1 r_h, the measurement errors are below 0.02 mag. Within r_h, field crowding (source confusion) results in slightly larger photometric measurement errors.

Table 1
Main Properties of the 14 Clusters in the Current Sample

Name	Alt. Name	R.A.$_{J2000}$ [a] deg	Decl.$_{J2000}$ [a] deg	$\bar{\mu_\alpha}$ [b] mas yr^{-1}	$\bar{\mu_\delta}$ [b] mas yr^{-1}	r_h [a] arcmin	m_V [a] mag	M_V [a] mag	$E(B\text{-}V)$ [a] mag	R_{GC} [a] kpc	[Fe/H] [a] dex
NGC 6441		267.554	−37.051	−2.568	−5.322	0.57	7.15	−9.63	0.47	3.9	−0.46
NGC 6453		267.716	−34.599	0.165	−5.895	0.44	10.08	−7.22	0.64	3.7	−1.50
NGC 6528		271.207	−30.056	−2.327	−5.527	0.38	9.60	−6.57	0.54	0.6	−0.11
NGC 6540	Djorg 3	271.536	−27.765	−3.760	−2.799	0.9	9.30	−6.35	0.66	2.8	−1.35
NGC 6544		271.836	−24.997	−2.349	−18.557	1.21	7.77	−6.94	0.76	5.1	−1.40
NGC 6553		272.315	−25.908	0.246	−0.409	1.03	8.06	−7.77	0.63	2.2	−0.18
NGC 6569		273.412	−31.826	−4.109	−7.267	0.8	8.55	−8.28	0.53	3.1	−0.76
NGC 6624		275.919	−30.361	0.099	−6.904	0.82	7.87	−7.49	0.28	1.2	−0.44
NGC 6626	M28	276.137	−24.870	−0.301	−8.913	1.97	6.79	−8.16	0.40	2.7	−1.32
NGC 6637	M69	277.846	−32.348	−5.113	−5.813	0.84	7.64	−7.64	0.18	1.7	−0.64
NGC 6638		277.734	−25.496	−2.550	−4.075	0.51	9.02	−7.12	0.41	2.2	−0.95
NGC 6642		277.976	−23.476	−0.189	−3.898	0.73	9.13	−6.66	0.40	1.7	−1.26
NGC 6652		278.940	−32.991	4.750	−4.450	0.48	8.62	−6.66	0.09	2.7	−0.81
NGC 6656	M22	279.100	−23.905	9.833	−5.557	3.36	5.10	−8.50	0.34	4.9	−1.70

Notes.
[a] Values collected from Harris (1996)
[b] Values from Vasiliev (2019).

a "0" superscript in all figures, while references to BDBS apparent magnitudes and colors in the text below this point refer to the reddening-corrected values.

For typical BDBS fields, the median binned photometric errors in u, g, and i do not exceed $\sim$0.025 unless going fainter than 19 mag, which is not done in this paper. However, as shown in the right panel of Figure 1, cluster fields are an exception since they feature the dense GC cores where BDBS photometric errors are affected by crowding. Fortunately, as can be seen in the center panel of Figure 1, the majority of analyzed stars have errors well below 0.025 mag. Catalog sources with poor photometric measurement flags in any band are not included in our analysis. In this work, all photometric color errors are the quadratic sum of apparent magnitude uncertainties used to define the color.

2.2. Southern Bulge GC Sample

At least 26 GCs fall within the BDBS field, most of which belong to the bulge subpopulation (Zinn 1996), distinguished by high metallicity, disk-like orbits, and proximity to the Galactic Center (Ortolani et al. 1995; Barbuy et al. 1998; Bica et al. 2016; Kerber et al. 2018). In this paper, we focus on the 14 most massive ($M_V < -6.35$ mag) of these clusters, and tabulate their main properties in Table 1. The remaining 12 GCs in the BDBS footprint are either too faint to be reliably studied with the methods presented in this paper, or have not been conclusively established as GCs; however, they will be explored in forthcoming work. Many of the sample clusters are metal-rich ([Fe/H] > -1) and red ($B - V > 1$), while also being distinct from halo clusters because of their proximity to the Galactic bulge. Traditionally, metal-rich GCs distributed within 3 kpc of the Galactic Center were identified as part of the bulge/bar system (Frenk & White 1982; Minniti 1995; Côté 1999). More recently, Masseron et al. (2019) classified bulge clusters as those on highly bound orbits with apogalacticon of <3.5 kpc; however, they caution that accreted nuclear clusters of dwarf galaxies could also end up on bulge-like orbits due to dynamical friction. Comprehensive studies

that include dynamical information, age estimates, and cluster metallicity are needed in order to accurately classify bulge GCs. Pérez-Villegas et al. (2020) perform an orbital analysis of 40 Galactic GCs using Gaia EDR3 proper motions (PMs; Gaia Collaboration et al. 2018, 2021), RR Lyrae distances, and spectroscopic radial velocities in order to classify them as part of either the bulge, thick disk, inner halo, or outer halo. They find that NGC 6528, NGC 6540, NGC 6553, NGC 6569, NGC 6624, NGC 6626, NGC 6637, and NGC 6642 are likely main bulge clusters, while NGC 6441, NGC 6453, NGC 6544, and NGC 6652 are more likely members of the thick disk. Their results are inconclusive regarding NGC 6638 and NGC 6656. Massari et al. (2019) derive the origins for 151 Galactic GCs using Gaia EDR3 kinematic information plus age–metallicity relations, and except for NGC 6638 and NGC 6652, which they deduce are likely main bulge clusters, they are in agreement with Pérez-Villegas et al. (2020). Massari et al. (2019) conclude that NGC 6441, NGC 6453, and NGC 6544 are part of a low energy system that could not be associated with a known merger event, and NGC 6656 is a main disk GC. Therefore, 10 of the 14 sample GCs are likely Galactic main bulge clusters, three are of indeterminate origin, and one is part of the main disk. All 14 GCs are treated homogeneously in the analysis but non-bulge clusters are separately labeled in figures.

As illustrated in Figure 2, these bulge GCs are distributed uniformly over much of the multidimensional parameter space describing their main properties. In relation to the general population of clusters from Harris (1996) (gray points), the sample clusters span nearly the entire range of absolute magnitudes, concentration parameter, and core relaxation time. Therefore this study probes the MP phenomenon in clusters spanning a wide range in structural parameters. On the other hand, these clusters are preferentially metal-rich, compact, red, and at small Galactocentric distances. Any systematic difference in the appearance of the MP phenomenon between these clusters and those of the halo might be related to their distinct inner Galaxy environment.

2.3. Gaia Matching and PM Cluster Membership Criterion

The BDBS point-source photometry used in this project is from the most recent BDBS-Gaia EDR3 (Gaia Collaboration et al. 2018, 2021) crossmatched catalog (Marchetti et al. 2022). We start by collecting BDBS-Gaia EDR3 crossmatched point sources from within 10 half-light radii (r_h) of each cluster center. The cutoff radius of $10r_h$ was chosen since we then include a large number of field stars in our preliminary selection, which are needed in order for cluster stars to be distinguished from field stars based on PMs: a well-populated PM vector point diagram is required for our Gaussian mixture modeling approach to work properly. Additionally, $10r_h$ is large enough that we can be certain most cluster stars are included in the analysis. The Gaia EDR3 point-source coordinates were back-propagated from J2016.0 (Gaia EDR3 astrometry) to J2013.99 (mean epoch of the BDBS observations), using Gaia EDR3 PMs. At this point, the two catalogs were crossmatched by selecting the nearest Gaia EDR3 point source within $1''$ of the BDBS sources. Table 2 is a correspondence table between the total number of BDBS sources versus the number of Gaia EDR3-matched sources in each of the $10r_h$ cluster fields. About 40% of the BDBS point sources in each cluster field were found to have corresponding Gaia EDR3 sources, although this figure varies between 21% and 78%, depending on the cluster. For the general BDBS field, the Gaia DR2 completeness is excellent to $i = 18$ (Rich et al. 2020) and better for EDR3. Additionally, Gaia EDR3 suffers much less from crowding in the GC cores than DR2. For most of the target GCs, the surface density of BDBS sources in the core is less than that for Gaia EDR3. Whereas the Gaia DR2 match rate was found to correlate significantly ($r = -0.83$) with Galactic latitude such that the Gaia-match is more complete for clusters at higher latitude, the correlation is much more modest ($r = -0.33$) for Gaia EDR3, due to better performance in crowded regions.

With the Gaia-matched catalog in hand, it was possible to create PM vector point diagrams for each cluster field, which were used to identify cluster members. We select stars within $\sqrt{\mu_\delta^2 + \mu_\alpha^2 \cos^2(\delta)} \leqslant 1$ mas yr^{-1} from the cluster mean PM coordinates (Vasiliev 2019), and tag these stars as candidate cluster members. Generally, the rms dispersion in the cluster PM distributions is different than 1 mas yr^{-1} (Rossi et al. 2015; Vasiliev 2019), and for most of the clusters the PM distributions overlap the field significantly. No choice of PM threshold could overcome the dual problem of undersampling the cluster and introducing field contaminants. We opted to choose a conservative PM radius to reduce contamination at the cost of missing cluster members. For a majority of the sample, the choice of a 1 mas yr^{-1} threshold represents less than 2σ in the mean dispersion in the distribution of PMs, which can be seen in Appendix. Exceptions are NGC 6544 and NGC 6656, which have PM distributions significantly offset from the field stars. For these two clusters we elected to use a 3 mas yr^{-1} threshold corresponding to 3σ from the cluster mean PM. For NGC 6441 and NGC 6528, which have PM distributions centered very near to the field population, we chose conservative thresholds of 0.5 and 0.67 mas yr^{-1} ($\sim 1\sigma$), respectively.

2.4. Comparing Member Surface Density with Gaia

We measured the radial surface number density profiles of the target clusters using both the BDBS point-source catalog and the Gaia EDR3 catalog. Figure 3 shows radial surface number density profiles for Gaia sources (blue squares) and BDBS sources (red squares). The purple profiles show the surface density ratio of BDBS versus Gaia (ticks on right-hand-side vertical axes). The densities were measured inside concentric radial bins of width $0.'5$, and the profiles were traced out to $10r_h$ in all cases. All of the radial surface density profiles (except for in the case of NGC 6652) show a similar pattern: the BDBS surface density peaks usually within $1'$ or $2'$ and decreases outward. For approximately half of the clusters, BDBS is most dense in the smallest radial bin, otherwise, the peak is farther out and BDBS is less dense than Gaia in the innermost regions. The shape of the profile does not correlate well with cluster extinction, Galactic latitude, or concentration parameter. However, the peak surface number density value is well correlated with cluster extinction, in the sense that BDBS has a higher point-source density (and even more so than Gaia in several cases) when the extinction is low. NGC 6652 has the lowest extinction in the sample and shows an inverted pattern, where the surface density ratio is greater beyond $1'$.

While the fraction of stars matched to Gaia DR2 within $10r_h$ of each cluster was significantly anticorrelated with Galactic latitude, the fraction of Gaia EDR3-matched BDBS stars was not. This is likely due to the completeness improvement of

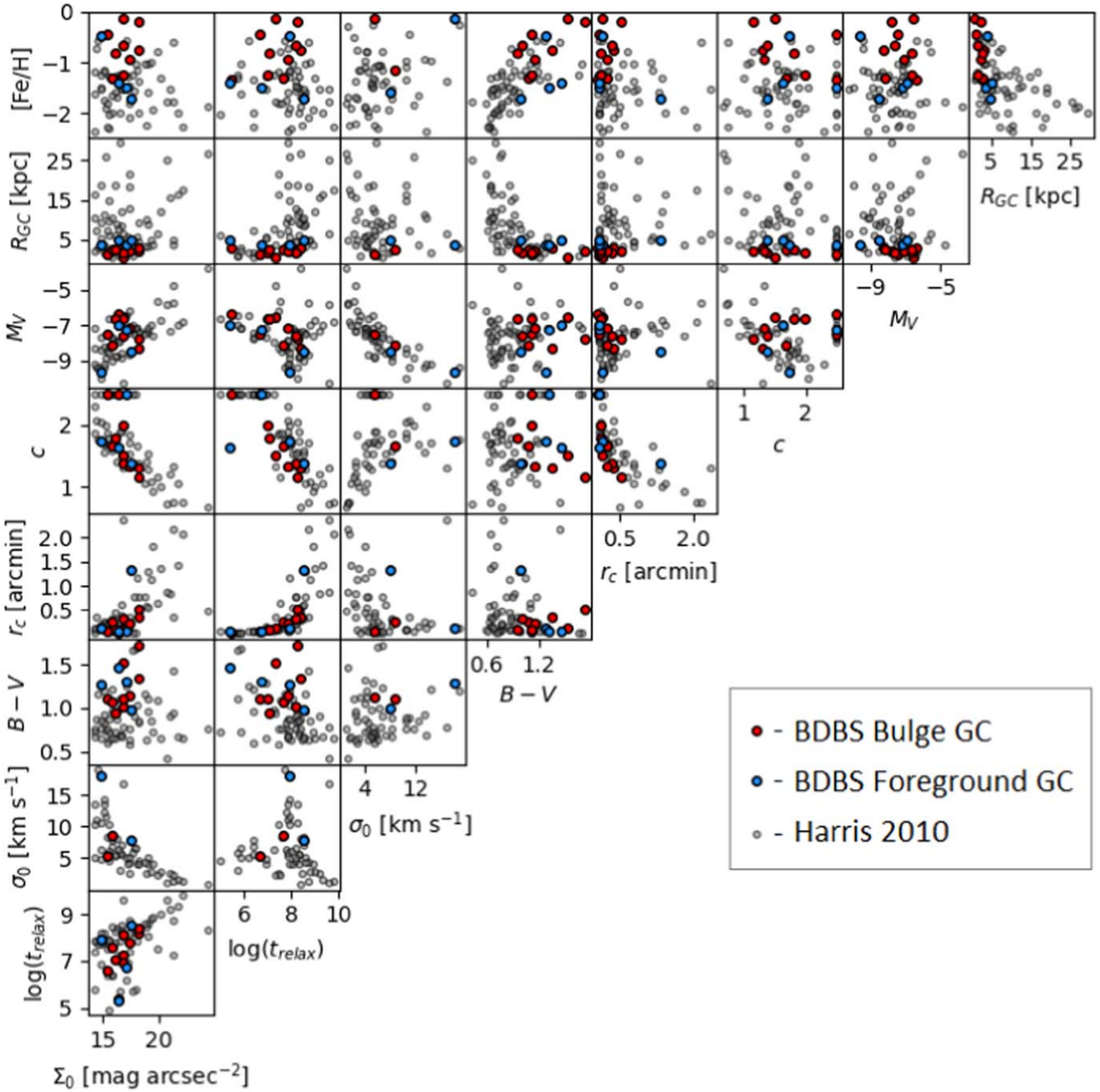

Figure 2. Parameter space plot showing the global properties of a representative sample of the overall Galactic GC population from Harris (1996) (gray circles), as well as for the 14 clusters in the present sample which are colored red if they are part of the bulge subpopulation of GCs, or blue if they are part of another system, e.g., interlopers or foreground thick disk clusters. The current sample spans the parameter space uniformly except for in R_{GC}, metallicity and color.

Gaia EDR3 versus DR2 in crowded fields (Gaia Collaboration et al. 2021). Across the sample of clusters we find a match rate with Gaia EDR3 ($N_{\rm Gaia-matched}/N_{\rm BDBS}$) of 0.43 ± 0.12.

We tested whether the differences in radial surface density profiles between BDBS and Gaia might have affected our derived global population ratios by repeating our analysis when stars inside $1'$ were excluded. For all clusters, we find that to within 1σ, the derived global population ratios were the same when excluding stars inside $1'$. We note that this is not unexpected, since we are computing the relative ratios of stars that are in the same cluster and span the same magnitude and radial ranges. However, since the surface density of BDBS point sources was significantly diminished inside $r = 1'$ for NGC 6441, NGC 6624, NGC 6652, and NGC 6656, stars inside that radius were excluded from the analysis of those clusters.

2.5. Selecting RGB Stars

We utilized an interactive polygonal selection region to visually select RGB stars in one of several color–magnitude diagram (CMD) planes, using the filter combination that best separated the RGB from the subgiant branch (SGB), horizontal branch (HB), and AGB stars. It was found that for all of the clusters, the r versus $u - r$ CMD sufficiently separated the RGB from the rest of the cluster stars. For the metal-rich clusters, it was not possible to separate the red HB from the RGB with any filter combination.

Table 2
Number of BDBS Sources Compared to the Number of Gaia EDR3-matched BDBS Stars within 10 r_h of Each Cluster

Cluster	b [deg]	N_{BDBS}	$N_{Gaia-matched}$	Match Rate
NGC 6441	−5.006	46,276	15,772	0.341
NGC 6453	−3.872	26,539	21,002	0.791
NGC 6528	−4.174	22,993	6,910	0.301
NGC 6540	−3.313	131,274	41,275	0.314
NGC 6544	−2.204	81,954	17,374	0.212
NGC 6553	−3.030	155,292	50,861	0.328
NGC 6569	−6.681	59,810	29,478	0.493
NGC 6624	−7.913	69,510	29,639	0.426
NGC 6626	−5.580	574,036	206,008	0.359
NGC 6637	−10.269	46,161	20,236	0.438
NGC 6638	−7.193	13,132	10,143	0.772
NGC 6642	−6.439	68,823	24,735	0.359
NGC 6652	−11.377	12,306	6,423	0.522
NGC 6656	−7.552	1,054,707	449,162	0.426

Note. The match rate does not correlate significantly with cluster Galactic latitude as was the case with Gaia DR2, likely because EDR3 is more complete than DR2 in crowded fields. We find an average overall match rate of 0.43 ± 0.12.

Figure 4 illustrates the process of selecting red giants in NGC 6626. We first queried the BDBS-Gaia EDR3-matched source catalog using a cone search with a radius of $10r_h$ for the cluster. The source position surface density is plotted in panel A (blue is more dense). In panel B we show the PM vector point density diagram for the same stars, zoomed into the vicinity around the mean PM of the cluster itself (red cross), from Vasiliev (2019). A concentration of points is evident at the location of the cluster mean PM, and the selection region described in Section 2.3 is shown as a black circle. Stars with PM $\leqslant 1$ mas yr^{-1} from the mean cluster value are indicated as black points in panels A and C. Panel C shows the r versus $u-r$ CMD for all Gaia EDR3-matched sources from within $10r_h$ of the cluster center and PM selected cluster members in black. The black points follow the bright end of the MS, SGB, RGB, AGB, and the extended blue HB of NGC 6626. Figure 4 illustrates that the PM matching minimizes contamination from stars of the Galactic bulge RGB and MS ($u-r \gtrsim 2$, $r \gtrsim 14$) and the Galactic disk MS ($u-r \lesssim 2$, $r \lesssim 17$), although it can be seen that there is field star contamination where these sequences intersect redward of the cluster MS, possibly due to Gaia EDR3 mismatches at the faint end where the BDBS astrometry has larger uncertainties.

In Figure 5, we show again the star selection process, but for the extremely metal-rich NGC 6441, which has a well-populated HB that is very red and intersects the RGB. Several other metal-rich clusters have red HBs (RHBs), which we later remove from the cluster RGB sample. This CMD shows that NGC 6441 also has a blue HB which forms a long tail. For NGC 6441, we used a more conservative PM selection radius of 0.5 mas yr^{-1} since the cluster PM distribution is concentric with the field star PMs.

3. Analysis

In this section, we discuss the methods used to identify multiple stellar populations on the RGBs of each cluster. The RGB stars were plotted in g versus C_{ugi} space (pseudo-color–magnitude diagrams) then the RGB was rectified and the ensuing histogram of RGB C_{ugi} pseudo-colors was evaluated. In all cases, the distributions were clearly non-Gaussian and in several cases the distributions were bimodal, or trimodal in the cases of NGC 6441, NGC 6626, and NGC 6656. An expectation-maximization (EM) algorithm was used to find the best-fitting Gaussian mixture model to the C_{ugi} distributions. We ran this algorithm 1000 times for each cluster while varying the rectifying parameters and randomizing the photometric magnitudes based on the photometric errors.

In all cases except for NGC 6441, NGC 6626, and NGC 6656, we find the best-fitting mixture model had two components. 1P stars were identified with the bluer Gaussian component while the 2P stars were identified with the redder Gaussian component.

3.1. Decontaminating the RGB

The cluster RGBs were cleaned of contaminating populations such as RHB and AGB stars in a straightforward and easily reproducible manner. We estimate the mean g magnitude of the RHB, g_{RHB}, by eye, and then clip stars with g magnitudes falling between $g_{RHB} \pm \Delta g_{RHB}$, where Δg_{RHB} is half the width (in g magnitudes) of the clipped portion of the RGB. Cluster RHB magnitudes and widths (g_{RHB}, $2\Delta g_{RHB}$) were (17, 0.75), (16.1, 0.75), (15.4, 1), and (16.6, 0.75) for NGC 6441, NGC 6528, NGC 6553, and NGC 6569, respectively. To remove AGB cluster stars, or remaining noncluster stars, we use σ-clipping. This is a simple procedure where the median and standard deviation of the C_{ugi} colors are computed in magnitude bins, and stars with colors outside two standard deviations from the median C_{ugi} value in the bin are clipped. For all clusters, we vary the number of σ-clips, N_σ, in the iterative model-fitting procedure.

3.2. Rectifying the RGB

With the cleaned RGB stars in hand, we rectified the RGBs using the algorithm from Milone et al. (2017, henceforth M17). First, the RGBs were divided into equal-width magnitude bins (Δg_{bin}). We used Δg_{bin} values between 0.1 and 0.15 mag. Fiducial points were placed at the 4th and 96th quantiles (blue and red edges) of the C_{ugi} color distribution in each magnitude bin. Then for each star, we defined the pseudo-color offset ΔC_{ugi}:

$$\Delta C_{ugi} = W_{C_{ugi}} \frac{X_{\text{fiducialR}} - X}{X_{\text{fiducialR}} - X_{\text{fiducialB}}}, \quad (1)$$

which is the local RGB-width-scaled offset from the red edge of the RGB, where $X = C_{ugi}$ and "fiducial R" and "fiducial B" correspond to the red and blue fiducial curves. $W_{C_{ugi}}$ is the width of the RGB measured as the separation between the red and blue fiducial lines two magnitudes brighter than the MSTO. If a cluster CMD was not deep enough to capture the MSTO, the magnitude of the bottom of the RGB was used. As with the RHB and σ-clipping described above, we included variations over the width of the magnitude bins ($\Delta g_{bin} = 0.1, 0.125, 0.15$) in the iterative model-fitting procedure. By iterating over magnitude bin widths we capture the dependence of the results on small changes to the fiducial curve shape in our uncertainty estimates.

The rectification process is illustrated in Figure 6. In panel A, the fiducial curves are colored red and blue, and the

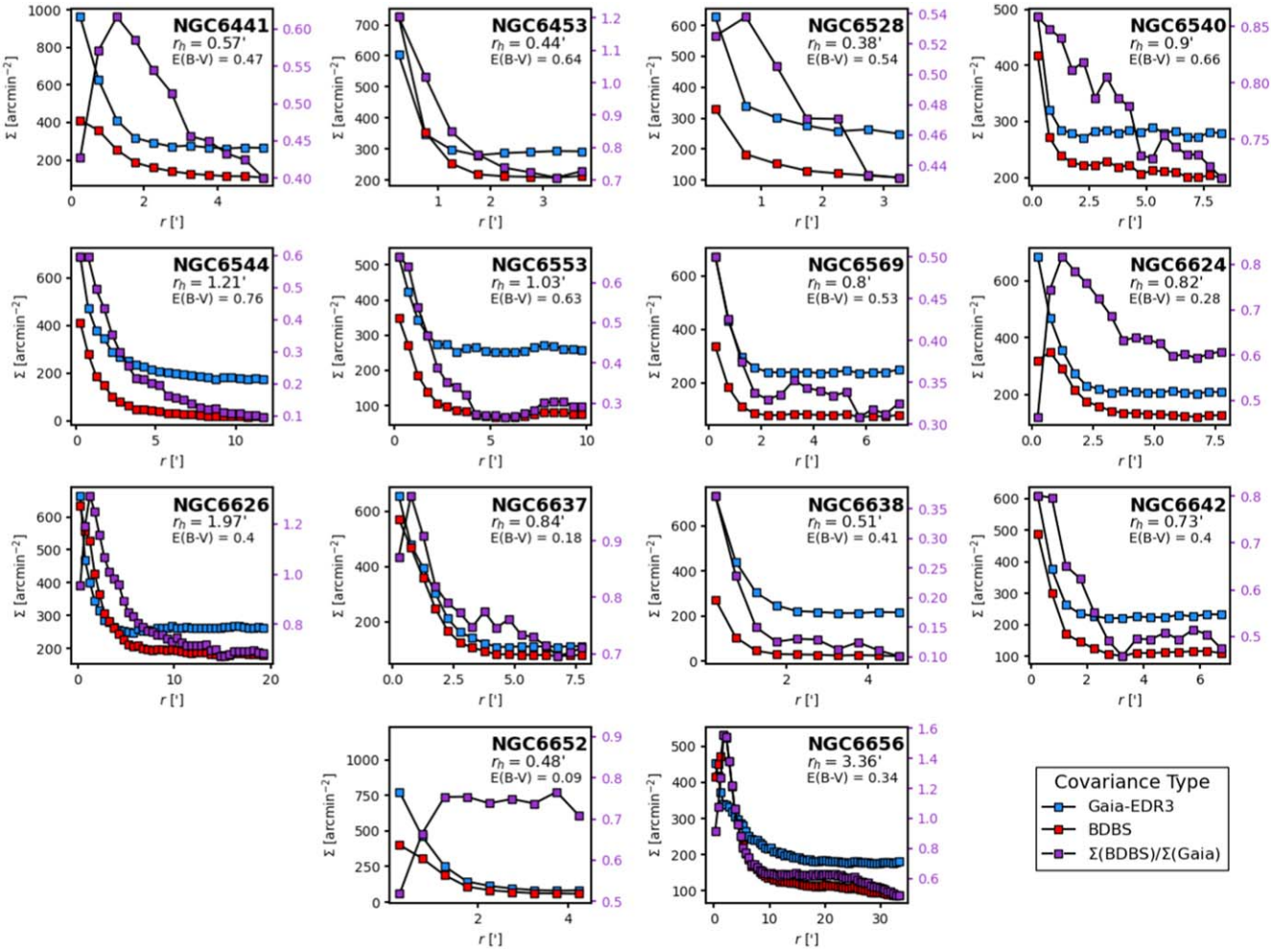

Figure 3. Surface number density profiles from the BDBS catalog (red) vs. Gaia EDR3 (blue). The stars were counted in 0.′5 wide circular bins extending out to $10r_h$ from the cluster center. For the majority of clusters, BDBS is on average less complete than Gaia EDR3, but the surface number density ratio improves with decreasing radii until $r = 1'$. Inside a radius of 1′, the surface number density of BDBS point sources either continues to improve or begins to decrease toward the center, depending on the cluster. The BDBS surface number density for NGC 6441, NGC 6624, and NGC 6652 diminishes significantly inside 1′. For NGC 6453, NGC 6626, NGC 6637, and NGC 6656, BDBS has a higher surface number density than Gaia EDR3 at, or interior to, r_h.

RGB width, $W_{C_{ugi}}$, is indicated by the green line, which in this cluster was measured at $g = 16.25$. After applying Equation (1) to all the RGB stars, we plot their ΔC_{ugi} values against their g-band magnitude in panel B, i.e., the rectified RGB. From this perspective, it is more clear that the RGB of NGC 6637 has two parallel sequences. The histogram of ΔC_{ugi} values across the entire g-band magnitude range is shown in panel C, along with a smoothed Gaussian kernel density estimation (KDE; green curve). The distribution of pseudo-color offsets is bimodal, suggesting that the RGB contains at least two stellar populations with distinct mean C_{ugi} colors.

The ΔC_{ugi} distributions of the rectified RGBs for all clusters in the sample are shown in Figure 7, complete with a smoothed Gaussian KDE to the distribution, where the bandwidth of the kernel is determined via Scott's rule of thumb (Scott 1979). A visual examination of Figure 7 reveals that the distributions are non-Gaussian. In many cases, the distributions were found to be bimodal (e.g., NGC 6453, NGC 6528, NGC 6624, NGC 6637, NGC 6638, and NGC 6642), while the remainder of the distributions are either significantly platykurtic or skewed. The ΔC_{ugi} distributions of NGC 6441, NGC 6626, and NGC 6656 are more complex, all giving the impression of three peaks.

Figure 7 also shows the color widths of the RGBs and the average photometric errors for the RGB stars (text at the top-left corner of each panel). The color width (σ) was calculated as the average rms dispersion in C_{ugi} colors across magnitude bins, where the uncertainty comes from the standard deviation in σ across the magnitude bins spanning the RGB. The mean C_{ugi} error, ε is also shown, averaged across the magnitude bins spanning the RGBs, where uncertainty in this quantity again comes from the standard deviation in ε across the magnitude bins. The C_{ugi} errors are computed as the quadratic sum of the individual errors in each of the three passbands u, g, and i. The average ratio $\varepsilon/\sigma = 0.17$, i.e., the color width of the RGBs was on average 6× that which could be expected if the broadening were due to photometric errors alone. The excess color widths σ were not found to be correlated significantly with Galactic latitude ($r = -0.04$, $p = 0.89$), which is an indication that the differential reddening corrections to the photometry were effective and do not contribute significantly to the RGB widths. We do find a mild (though not statistically significant) correlation between σ and M_V ($r = -0.29$, $p = 0.31$), suggestive of a mass-RGB-width relation.

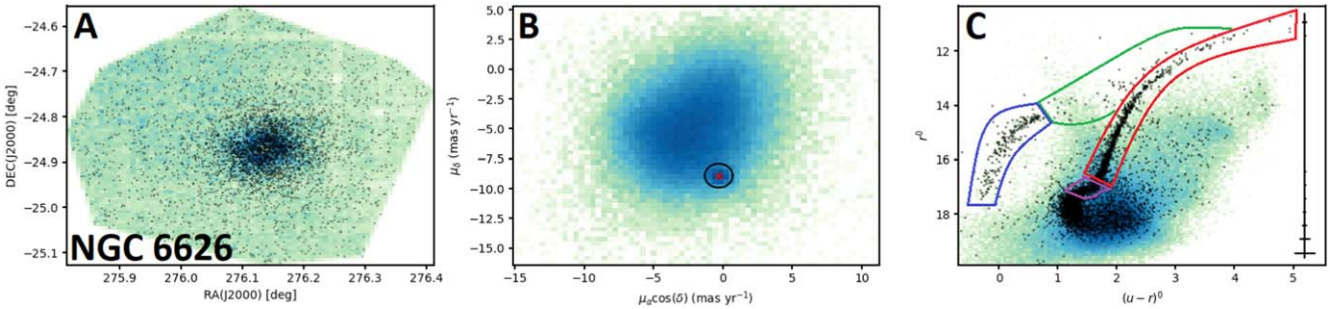

Figure 4. Selection of RGB stars from PM-matched cluster members for NGC 6626. RGB, AGB, SGB, and HB are enclosed red, green, purple, and blue in panel C. The stars enclosed in red were those selected for further analysis.

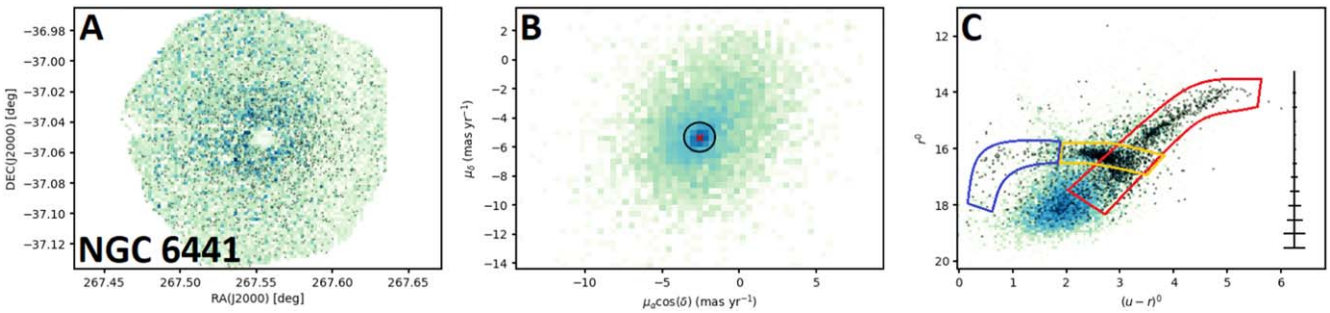

Figure 5. RGB star selection process for NGC 6441, which has a red HB (outlined in orange) that intersects the RGB.

3.3. Gaussian Mixture Models

We use Gaussian mixture models to identify and quantify the MPs underlying the pseudo-color distributions shown in Figure 7. In particular, we made use of the open-source software machine learning library `Scikit-Learn` (Buitinck et al. 2013), written in Python. The library contains many statistical clustering methods, including Gaussian mixture models. A Gaussian mixture model (GMM) is a function made up of several Gaussian probability distributions, each with an associated mean μ, covariance Σ, and mixing coefficient π. The equation that defines a GMM with K components is

$$p(\boldsymbol{x}_n) = \sum_{k=1}^{K} p(\boldsymbol{x}_n|z_k = 1)p(z_k = 1) = \sum_{k=1}^{K} \pi_k \mathcal{N}(\boldsymbol{x}_n|\mu_k, \sigma_k), \tag{2}$$

where $p(\boldsymbol{x}_n)$ is the probability of measuring $\boldsymbol{x}_n = \Delta C_{ugi,n}$ for star n, marginalized over all values $z_{n,k}$; z_k is unity if the star belongs to mixture component k and is zero otherwise; $p(\boldsymbol{x}_n|z_k = 1)$ is the probability of measuring $\boldsymbol{x}_n = \Delta C_{ugi,n}$ given that star n belongs to mixture component k; and $p(z_k = 1)$ is the unconditional probability of measuring a star that comes from component k. The last equality in Equation (2) is due to two facts: (i) that $p(z_k = 1)$ is just equal to the mixing coefficient π_k since the components are themselves probability distributions, and (ii) that $p(\boldsymbol{x}_n|z_k = 1)$ is simply equal to the Gaussian density function $\mathcal{N}$ that describes component k. Of interest here is the probability of a star belonging to one or another component, given its observed pseudo-color $\boldsymbol{x}_n$, that is, we want to know $p(z_k = 1|\boldsymbol{x}_n)$. Using Bayes equation and several of the definitions above, this may be written as

$$p(z_k = 1|\boldsymbol{x}_n) = \frac{\pi_k \mathcal{N}(\boldsymbol{x}_n|\mu_k, \Sigma_k)}{\sum_{j=1}^{K} \pi_j \mathcal{N}(\boldsymbol{x}_n|\mu_j, \Sigma_j)}. \tag{3}$$

The corresponding joint probability for all observations over all mixture components $p(\boldsymbol{X}, \boldsymbol{Z})$ is cast as the likelihood. The EM algorithm makes use of the likelihood in order to fit the mixture models to the ΔC_{ugi} distributions. The first step in the EM algorithm is to generate initial guesses to the mixture model parameters $\theta = \{\pi, \mu, \Sigma\}$, which is done using k-means clustering. Next is the expectation step, where the expectation of the log-likelihood is computed given the updated parameters θ^*:

$$\mathbb{E}[\ln p(\boldsymbol{X}, \boldsymbol{Z}|\theta^*)] = \sum_{n=1}^{N}\sum_{k=1}^{K} p(z_k = 1|\boldsymbol{x}_n) \times [\ln \pi_k + \ln \mathcal{N}(\boldsymbol{x}_n|\mu_k, \Sigma_k)]. \tag{4}$$

In the maximization step, an updated set of model parameters is found using maximum likelihood, i.e., the derivative of Equation (4) is set to zero and solved in terms of the parameters μ_k and Σ_k. These are then used in a new expectation step. The process iterates until the gain in the expected log-likelihood is below a convergence threshold of 10^{-3}.

For each cluster, we reinitialize the rectified RGB 1000 times. For each realization, the stellar magnitudes are randomized by drawing a new magnitude for each star from a Gaussian distribution with mean and standard deviation equal to the apparent magnitudes and errors on the apparent magnitudes, respectively. We also include variations over N_σ and $\Delta g_{\rm bin}$. For each realization, we fit four Gaussian mixture models, each with a different number of components ($N = 1-4$). For each value N, we initialize the model using k-means clustering to estimate the centroids of the N components. We estimate the component parameters in each case using the EM algorithm. For each value N, we find the maximum-likelihood mixture model for the *tied*, *diagonal*, *spherical*, and *full* covariance cases. For univariate distributions, a Gaussian mixture model that has tied, diagonal, or spherical covariance has

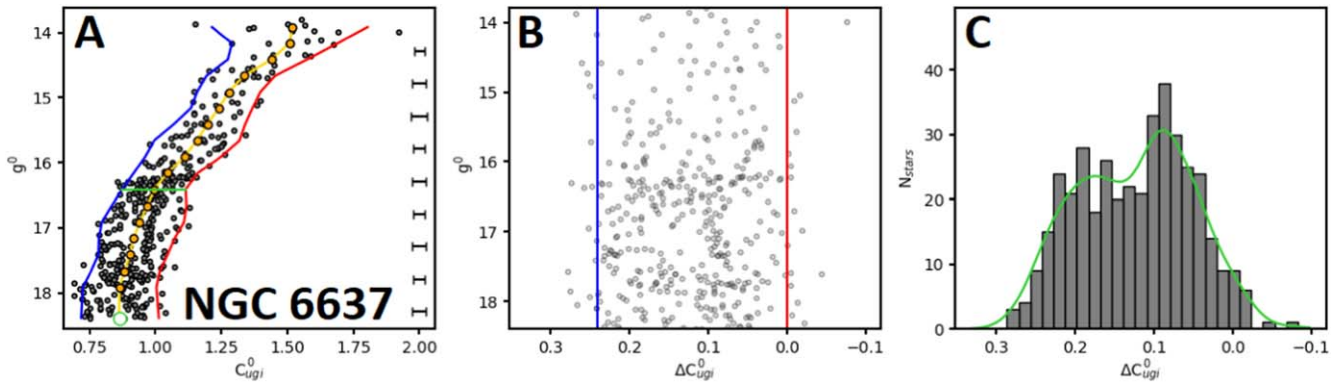

Figure 6. The three panels illustrate the process for rectifying the RGB for NGC 6637. The red and blue curves in panel A are the 4th and 96th percentiles (edges) of the RGB and the width of the RGB is measured at the location of the green line segment. The orange continuous curve is the median fiducial curve of the RGB, determined at discrete magnitude bins (orange circles). The green circle indicates the faint limit of our analysis of NGC 6637. Photometric errors in C_{ugi} as a function of g magnitude are indicated as bars to the right of the RGB. The rectified RGB is shown in panel B for the same magnitude range as in panel A. Panel C shows the distribution over rectified C_{ugi} colors (pseudo-color offset, ΔC_{ugi}) of the RGB stars. A Gaussian KDE of the distribution is shown in green. The histogram in panel C reveals bimodality in the pseudo-color offset distribution, indicating multiple, parallel subsequences on the RGB.

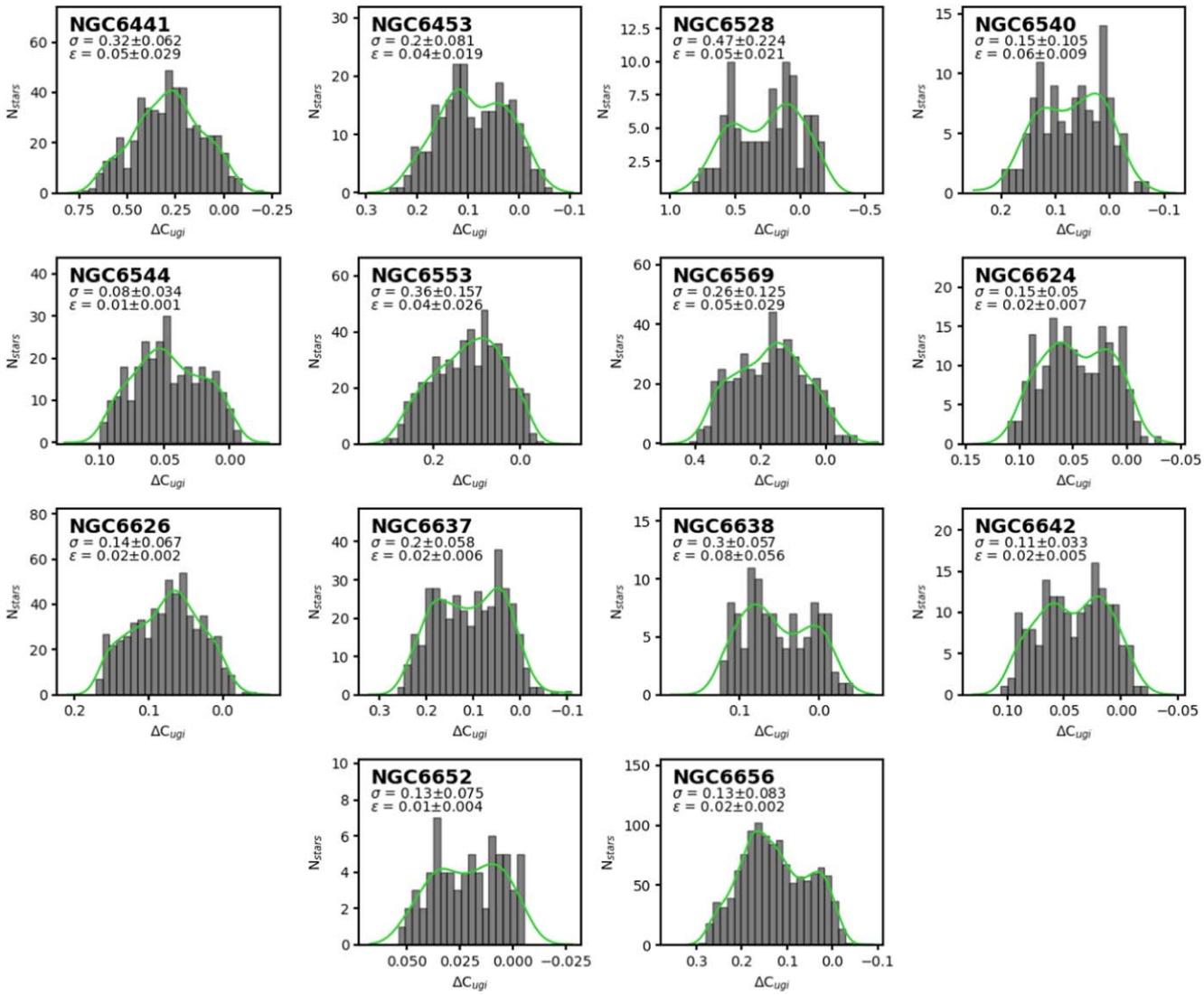

Figure 7. These histograms show that the ΔC_{ugi} distributions for the RGB stars in the sample clusters are in all cases skewed, platykurtic, or multimodal, indicating that the RGBs of the clusters are comprised of at least two stellar populations with distinct light element abundances. The green curves are Gaussian KDEs of the distributions, with kernel widths determined via Scott's rule. The average RGB widths across the sample of GCs were found to be $\sim 6\times$ the value expected from photometric errors alone.

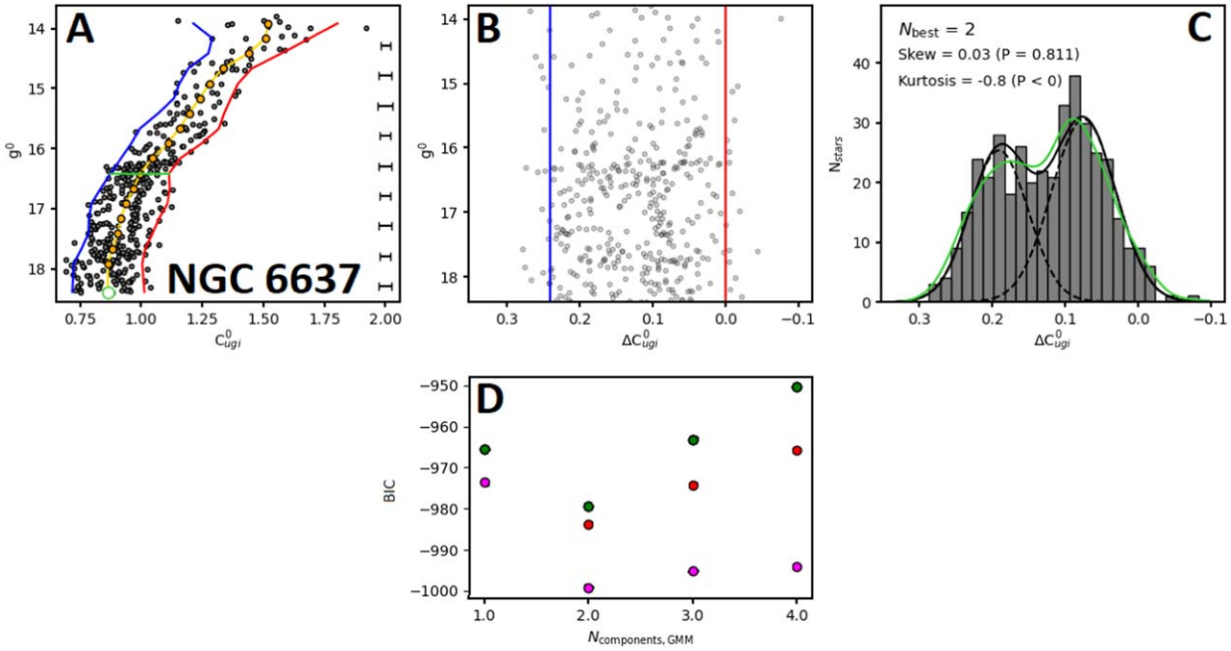

Figure 8. Snapshot of the mixture model-fitting algorithm in action for NGC 6637. Panel A shows the RGB of the cluster in g vs. C_{ugi} space, as well as the red and blue fiducial curves and the location of the RGB-width $W_{C_{ugi}}$ measurement (green line). Panel B shows the rectified RGB. Panel C shows the pseudo-color distribution of the rectified RGB, the smoothed Gaussian KDE in green, the Gaussian mixture model components as dashed curves, and the sum of the model components as the solid black curve. We show the skewness and kurtosis values of the distribution along with the p-value of a student t-test. The two-tailed t-test assumes a Gaussian shape to the distribution as the null hypothesis, which is rejected given extreme enough skew or kurtosis, using a 0.05 significance level. Panel D shows the BIC for the different covariance mixture models: tied covariance models are red while spherical, diagonal, and full covariance models overlap in this realization, and are colored green. The full covariance model was also scored using the AIC, shown in magenta.

components with equal Gaussian dispersion σ. Univariate Gaussian mixture models with full covariance have components with σ-values that are allowed to vary with respect to one another.

For each resampled ΔC_{ugi} distribution, we determine the optimum number of Gaussian components for the distribution using the Bayesian information criterion (BIC), which is computed for each Gaussian mixture model (with different combinations of N components and covariance types). The BIC scores the mixture model based on the goodness of fit in a maximum-likelihood sense but also includes a term that penalizes overfitting.

Figure 8 illustrates our use of the BIC in order to determine the optimum number of Gaussian components for the given distribution, in this case, the rectified RGB of NGC 6637. The value of the BIC was computed for each model at each iteration (realization of the RGB). In panel D, we see the BIC computed for models with $N = 1-4$ components, for each covariance type (color coding described in the caption of Figure 8). In this realization, the spherical, tied, and diagonal cases have nearly the same BIC score since the covariance in a univariate mixture is a single number per component, rather than a matrix. However, since we initialize the GMM using k-means clustering, and since the clustering itself has random initial centroids, the spherical, tied, and diagonal models may result in slightly different Gaussian component means and covariances. Larger negative values of the BIC indicate better fits to the distribution. In panel D it can be seen that the Aikake information criterion (AIC; magenta-filled circles) used in addition to BIC to score the full covariance models, and the BIC shows a clear minimum at $N = 2$ for all covariance types. The best-fit N, which we refer to as $N_{\rm best}$, is defined as the location of the minimum BIC value. For each realization, we use a two-tailed student t-test (with a significance level of 0.05) to evaluate whether the hypothesis of a normal distribution over ΔC_{ugi} can be rejected given sufficiently extreme skew or kurtosis. Mixture models with a single component are rejected when the t-test fails, and the next best model (as measured with the BIC) is chosen. After completing the analysis for 1000 realizations of the rectified RGB, we investigate the distribution of $N_{\rm best}$. In all cases, we find that $N_{\rm best} = 2$ is the most frequent result, except for NGC 6441, NGC 6626, and NGC 6656, for which we find $N_{\rm best}$ is most frequently found to be 3.

3.4. Computing Population Ratios

From the Gaussian fits to the ΔC_{ugi} distributions, we seek to recover the fraction of 1P stars on the RGB. We define the population ratio $N_1/N_{\rm tot}$ as the number of stars belonging to the blue component (larger positive ΔC_{ugi}), divided by the total number of stars on the RGB. Our identification of stars with smaller (bluer) C_{ugi} values as the Na-poor population (1P) follows from Lardo et al. (2011), who find that the spread in $u - g$ colors correlates with Na abundance in such a way that Na-poor stars are bluer in $u - g$. This is similar to the $U - B$ index, where stars poor in sodium and nitrogen are bluer in $U - B$. Additionally, the $g - i$ index is expected to behave in a similar way to $B - I$, where He- and Na-poor stars are found to be redder (Monelli et al. 2013). Therefore in the pseudo-color index C_{ugi}, 1P stars are bluer than the Na-enhanced 2P. ΔC_{ugi} is defined in such a way that stars increasingly bluer in C_{ugi} have more positive ΔC_{ugi} values, and very red stars will have small or negative ΔC_{ugi} values.

When fitting a Gaussian mixture model one can adopt a Bayesian framework whereby each data point has a posterior probability associated with belonging to either component, i.e., $P_1 = p(z_1 = 1|x_n)$ refers to the probability that the star belongs to component 1, and $P_2 = p(z_2 = 1|x_n)$ is the probability that the

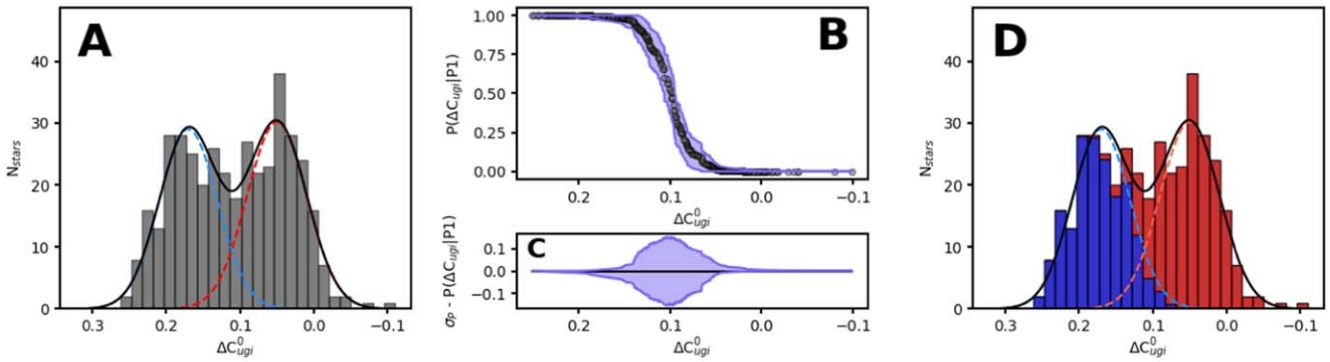

Figure 9. Population ratio derivation for NGC 6637, according to the best-fit Gaussian mixture model. Panel A shows the ΔC_{ugi} histogram of the rectified RGB with mixture model components superimposed in blue (1P) and red (2P), with their sum as the solid black curve. Panel B shows the posterior probability of membership to 1P as a function of ΔC_{ugi}. The magnitude of the error envelope is shown in panel C, where it is evident that the largest uncertainties on the membership probability occur where the components overlap. Panel D shows the ΔC_{ugi} histogram again but is now color coded to reflect the membership of stars to the two components as a function of ΔC_{ugi}.

star belongs to component 2. We explored three definitions for N_1: stars with $P_1 \geqslant 0.65$, stars with $P_1 \geqslant 0.5$, and a third approach that divides the pseudo-color distribution into bins, computes the average values of the probabilities among the stars in each bin ($\langle P_1 \rangle$ and $\langle P_2 \rangle$), and divides the stars in each bin into the two populations according to relative amplitude of $\langle P_1 \rangle$ versus $\langle P_2 \rangle$ (see Figure 9, panel D). In this third method, we normalize the probability density function of each mixture model component, then renormalize both to the maximum frequency of the histogram. Considered over the width of a histogram bin, the relative amplitude of the two probability distribution functions (PDFs) at the value of the bin center can be interpreted as a relative probability. If, for instance, the two PDFs have the same height in a bin, then the stars in the bin are evenly divided between each of the two populations. Unsurprisingly, the result derived in this method is somewhat dependent on the choice of bin size, but the dependence is weak after at least 25 bins are used.

3.5. Uncertainties on the Population Fractions

The RGB rectification procedure involves a couple of tunable parameters that can affect the shape of the ΔC_{ugi} distributions. The parameters are the width of the magnitude bins, $\Delta g_{\rm bin}$, used to define the red and blue fiducial curves and the number of σ-clipping iterations used, N_σ. Variations in these parameters affect the shape of the distributions in a nonrandom way, but since it is not clear which parameter combination is the *right* one, we opt to iterate over many and take the median and standard deviation of the derived $N_1/N_{\rm tot}$ as a measure of the population fraction and the associated uncertainty that arises from these systematics. We find that the systematic uncertainties were on the $\sim$10% level, or about 60% of the statistical error associated with photometric errors. Again, the photometric errors were folded in as a measure of statistical uncertainty by randomizing the apparent magnitudes based on their associated errors for all the stars during each iteration of our model-fitting process, which contributes to the final dispersion in $N_1/N_{\rm tot}$ that is used to compute the total uncertainty $\Delta {\rm N}_1/{\rm N}_{\rm tot}$.

The overall uncertainty in our resulting $N_1/N_{\rm tot}$ fractions also has a contribution from the probability-weighted integration technique described in the previous section, since the method relies on a probabilistic rather than deterministic definition of N_1 membership. We quantify this uncertainty by simulating 1000 random draws from a binomial distribution that has a success rate equal to the value of the blue PDF at each ΔC_{ugi} value. In Figure 9, panel B, we show the posterior probability of 1P membership for each red giant star in NGC 6637, as a function of ΔC_{ugi} offset. The purple envelope comes from the $\pm 3\sigma$ values from the distribution of 1000 random binomial draws for each star. The median 3σ value across the entire ΔC_{ugi} distribution serves as the uncertainty in our result caused by the probabilistic nature of our definition of N_1. As can be seen in Figure 9, panel C, the greatest uncertainty on the membership probability occurs in the region of overlap between the two Gaussian components. The uncertainty stemming from the probability-weighted integration technique accounts for $\sim$30% of the total uncertainty on the $N_1/N_{\rm tot}$ values. The total uncertainty on the population fractions, $\Delta N_1/N_{\rm tot}$, is computed as the quadratic sum of the uncertainties that stem from bootstrapping the fit parameters, reinitializing the apparent magnitudes using their associated errors, and the uncertainty associated with the probabilistic nature of the probability-weighted integration technique. The median total percent error among the derived population fractions was 26%.

4. Results

In this section, we present our results, which include a measure of the confidence with which we find multiple subsequences along the RGBs of the clusters; the derived fraction of 1P stars in the RGB of each cluster; and comparisons between the population ratios and global cluster parameters, along with evaluations of the significance of any correlations found.

4.1. Number of RGB Components

Although the color distributions shown in Figure 7 are visually suggestive of multiply-populated RGBs, it is important to devise an independent and unbiased approach that might lead to the same conclusion. To this end, we fit Gaussian mixture models to the rectified RGB of each cluster 1000 times, each time resampling with the replacement of the stars of the RGB and varying the rectification parameters. For each realization, we record the value of $N_{\rm best}$ for each covariance type. Although, as discussed in Section 3.3, the tied, diagonal, and spherical covariance models use components with identical σ, they are initialized separately for each realization of the data,

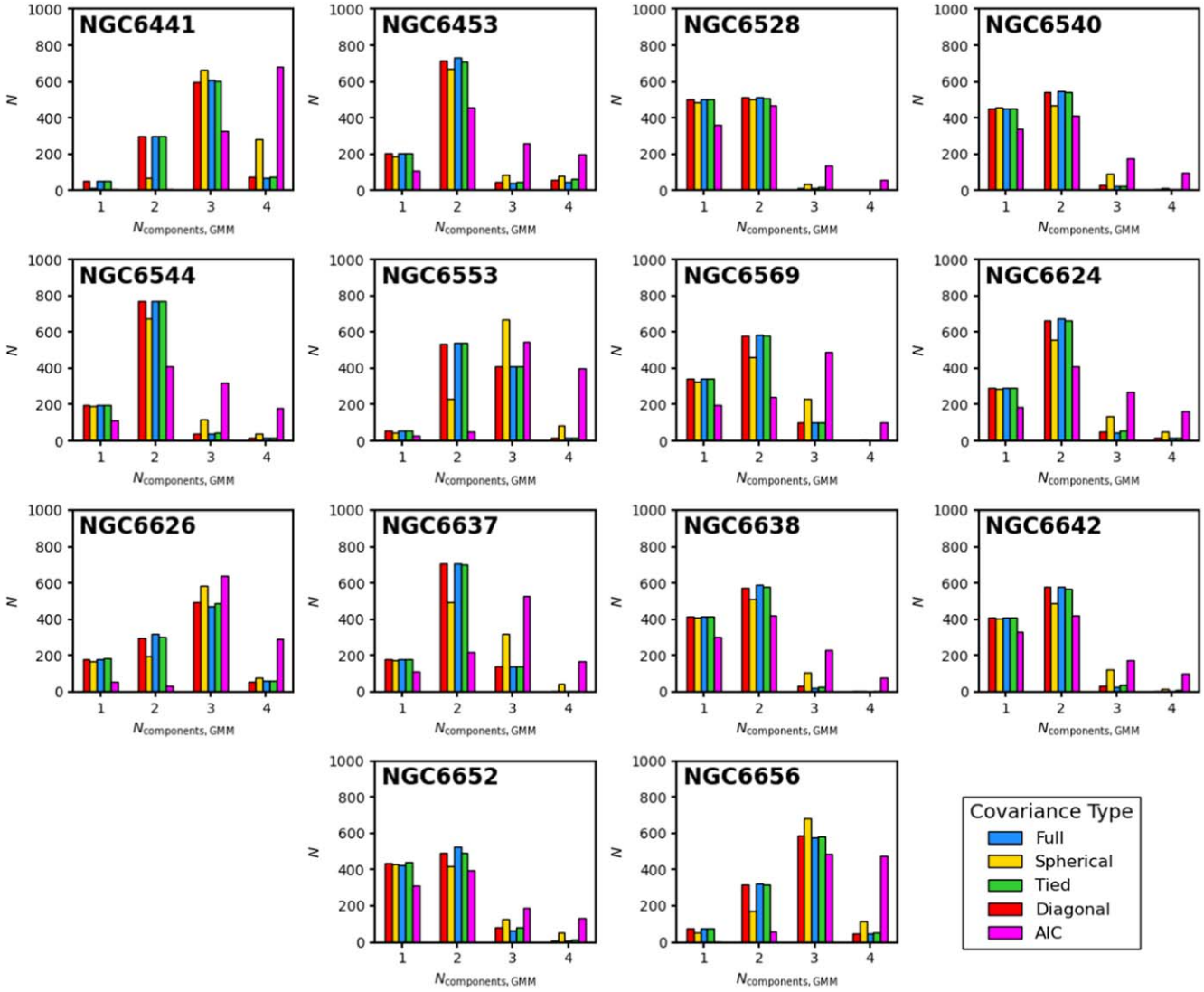

Figure 10. For each cluster, we show the histogram of N_{best} values after 1000 bootstrap resamples of the rectified RGB. In all cases, the histograms confirm multimodality in the ΔC_{ugi} distributions, with peaks at $N_{best} = 2$ or 3. The bars are color coded according to covariance type: red, green, yellow, and blue correspond to tied, diagonal, spherical, and full covariances, respectively. The AIC result is colored in magenta, and was computed for GMMs with full covariance. We conclude that NGC 6441, NGC 6626, and NGC 6656 harbor at least three populations.

and therefore serve as semi-independent models. As explained in Section 3.3, for each of the 1000 realizations of the rectified RGB we fit several Gaussian mixture models, each with a different number of components N, where $N = 1$–4. In Figure 10 we show a histogram of N_{best} values for each cluster. Considering full covariance models, we most frequently found $N_{best} = 2$, except for NGC 6441, NGC 6626, and NGC 6656, which were found to have $N_{best} = 3$ most frequently. We interpret this result as evidence suggesting all the sample GCs have at least two populations, although for NGC 6528, NGC 6540, and NGC 6652, $N_{best} = 1$ is almost as frequent, indicating further work will be needed in order to definitively rule out a single population scenario for these clusters. Figure 10 also demonstrates that N_{best} is most frequently found to be two for models of all covariance types, except for NGC 6553, where the spherical covariance models were best fit with three components. We also recorded the AIC for the full covariance models, represented in Figure 10 with magenta-colored bars. The AIC tends to find higher values of N_{best} more frequently than the BIC because it penalizes overfitting less strictly.

4.1.1. Three-component RGBs

Based on the findings presented in Figure 10, we conclude that three of the four most massive clusters in the sample, NGC 6441, NGC 6626, and NGC 6656, may harbor at least three populations. In the case of NGC 6656, such a finding is not unprecedented. There is continuing debate about whether NGC 6656 is an iron-complex cluster: Marino et al. (2011) find two stellar groups characterized by different mean [Fe/H] values, with an overall metallicity spread among the stars ($-2.0 \lesssim$ [Fe/H] $\lesssim -1.6$) that is positively correlated with slow neutron-process (s-process) element abundances (Marino et al. 2009, 2011, 2012). Additionally, Marino et al. (2011) report a sharp separation between two stellar groups based on s-process abundances, with both groups having Na-O and C-N anticorrelations. Group 1 (G1) is s-poor with $\langle$[Fe/H]$\rangle = -1.82$, and group 2 (G2) is s-rich with $\langle$[Fe/H]$\rangle = -1.67$. However, see Mucciarelli et al. (2015) who find no spread in [Fe/H] among stars in NGC 6656. Whereas Marino et al. (2009) report no discrete groups in their Na-O anticorrelations, the Hubble Space Telescope (HST) photometric *chromosome maps* of

M17 do reveal at least three different groups of stars on the RGB. More recently, Lee (2020) reported five populations among NGC 6656 red giants using narrowband Ca-CN-CH photometry: these were interpreted as two main groups with different metallicity, where the lower-Fe group is split into two subpopulations with different CN band strengths and the higher-Fe group was divided into three groups with weak, intermediate, and strong CN band strengths. Using the abundances from Marino et al. (2012), we find a significant difference in the C_{ugi} colors of SGB stars with differences in s-process elemental abundances (see Figure 23 in Johnson et al. 2020). We propose that the three observed C_{ugi} sequences reflect star-to-star variations in the light element abundances and s-process element abundances of RGB stars. Our interpretation of the C_{ugi} distribution for NGC 6656 is based on the Na-O anticorrelations for G1 and G2 RGB stars shown in Figure 14 of Marino et al. (2011). The P1 (bluest) component contains stars at the Na-poor end of the Fe-poor, s-poor group (G1) Na-O anticorrelation; the P2 (intermediate color) component contains stars from the Na-rich end of the G1 Na-O anticorrelation as well as stars from the Na-poor end of the G2 Na-O anticorrelation; and the P3 (reddest) component contains stars from the extreme O-depleted end of the G2 Na-O anticorrelation. Unfortunately, there are no stars with CNO,Na abundances from Marino et al. (2011) within 2″ of any of our sample cluster stars in NGC 6656. Therefore, more spectroscopic observations will be needed for direct comparison.

Using their HST photometry, M17 find dispersions in $C_{\rm F275W,F336W,F438W}$ and $m_{\rm F275W}-m_{\rm F814W}$ among NGC 6441 RGB stars that are substantially larger than expected from photometric errors, but do not separate the cluster into multiple discrete populations. On the other hand, Bellini et al. (2013) report two distinct populations in NGC 6441 since they find a clearly split RGB in the F390W—F606W color index. NGC 6441 has a peculiar HB morphology for a metal-rich GC, and the results of several studies suggest that populations with varying He abundance may be the cause (e.g., Caloi & D'Antona 2007; Yoon et al. 2008). Gratton et al. (2007) found that the [O/Na] distribution for the RGB stars in NGC 6441 is qualitatively well matched to the color/morphology of the HB, which was divided into three regions. The cluster does apparently harbor a very high helium population, including ∼10% of stars, as evidenced by the high-$T_{\rm eff}$ extension of the HB (Busso et al. 2007; Caloi & D'Antona 2007; D'Ercole et al. 2008; Yoon et al. 2008). Additionally, Bellini et al. (2013) find a double MS in optical passbands, which they find is best explained by the presence of 2G stars that are enhanced in He. Stars that are enhanced in He are likely to explain both the peculiar HB morphology in metal-rich clusters, and the O depletion that is observed in some RGB stars (Carretta et al. 2009). The large collection of Na and O abundances compiled by Carretta et al. (2009) revealed that 2G stars are occasionally split into two subpopulations in very massive clusters. We suggest that by virtue of the sensitivity of C_{ugi} to He variations (Piotto et al. 2007; di Criscienzo et al. 2010; Monelli et al. 2013) that we have detected at least three populations in NGC 6441: the 1P stars, which are chemically similar to field stars, $2P_a$ stars, which are enhanced in C + N + O, and $2P_b$ stars, which are enhanced in C + N + O and He.

NGC 6626 is a very old, massive, metal-poor bulge GC, which is in many ways very similar to the more extensively studied NGC 6656 (Moni Bidin et al. 2021). Mauro et al. (2014) analyzed calcium triplet measurements to find a metallicity distribution that was wide, consisting of two peaks separated by ∼0.2 dex, but this has been contested by Villanova et al. (2017) and Moni Bidin et al. (2021) who both claimed no intrinsic metallicity spread. Work by Moni Bidin et al. (2021) indicates this cluster is tidally stressed and is losing mass into the bulge, and suggest the cluster is possibly a primeval bulge building block. This cluster is otherwise poorly studied and there are few spectroscopic clues from the literature as to the heavy or light elemental content of the cluster stars. The bluest 1P component appears to be very well separated from the rest of the stars in ΔC_{ugi} space, more so than in NGC 6441 and NGC 6656. It may be that the three components are due to light and s-process elemental abundance variations among cluster stars in a fashion similar to NGC 6656, but spectroscopic observations will be needed to test this hypothesis.

4.2. Derived Population Number Ratios

Figure 11 shows the ΔC_{ugi} distributions for each cluster RGB, overlaid with the best-fitting Gaussian mixture model. The value of $N_1/N_{\rm tot}$ was found to vary between 0.25 and 0.51 across the sample, in line with other studies (Wagner-Kaiser et al. 2016; M17; Lee 2019). The population ratio estimates have total uncertainties at the ∼26% level and are derived from repeating the population assignment procedure 1000 times while randomizing magnitudes based on photometric errors and varying the parameters used to rectify the RGBs. The population fractions reported in Table 3 and shown in Figure 11 are the median value from the iterative process. The ΔC_{ugi} distributions shown in Figures 7 and 11 are single realizations of the iterative process described above (without randomizing the magnitudes), and were picked because they are quantitatively and visually representative of the ensemble of ΔC_{ugi} distributions for each cluster RGB.

4.3. Literature Comparisons

For several clusters in the sample, photometric population tagging and/or spectroscopic light element abundance determinations are available in the literature. Population fractions for four of the sample clusters were also derived by M17 and we present their results alongside our own in Table 3. Our results are in modest agreement with M17 except for NGC 6624, where M17 find significantly fewer 1P stars. We do not find better agreement with M17 when we restrict our study to a field with the same angular size for NGC 6624, NGC 6652, and NGC 6656.

The large UV-optical HST photometric data set collected by Piotto et al. (2015) for many Galactic GCs is a useful point of comparison for our results. In Figure 12 we show comparisons between HST *magic trio*-selected populations and our own C_{ugi}-selected populations. The HST CMDs for NGC 6624, NGC 6637, NGC 6652, and NGC 6656 all have clearly split RGBs and we select by hand the individual sequences. After matching the two data sets spatially using a 0.5″ search radius, we plot the C_{ugi} colors of each matched star and find that the HST 1G and 2G stars are blue and red in C_{ugi}, respectively, for NGC 6624, NGC 6637, and NGC 6652. The HST CMD for NGC 6656 was split into three sequences, stars from which were found to have distinct C_{ugi} colors on average. Since the ground-based C_{ugi} CMDs are not as clearly split as the HST CMDs, it was necessary to verify our GMM population identification technique in a comparison such as this one.

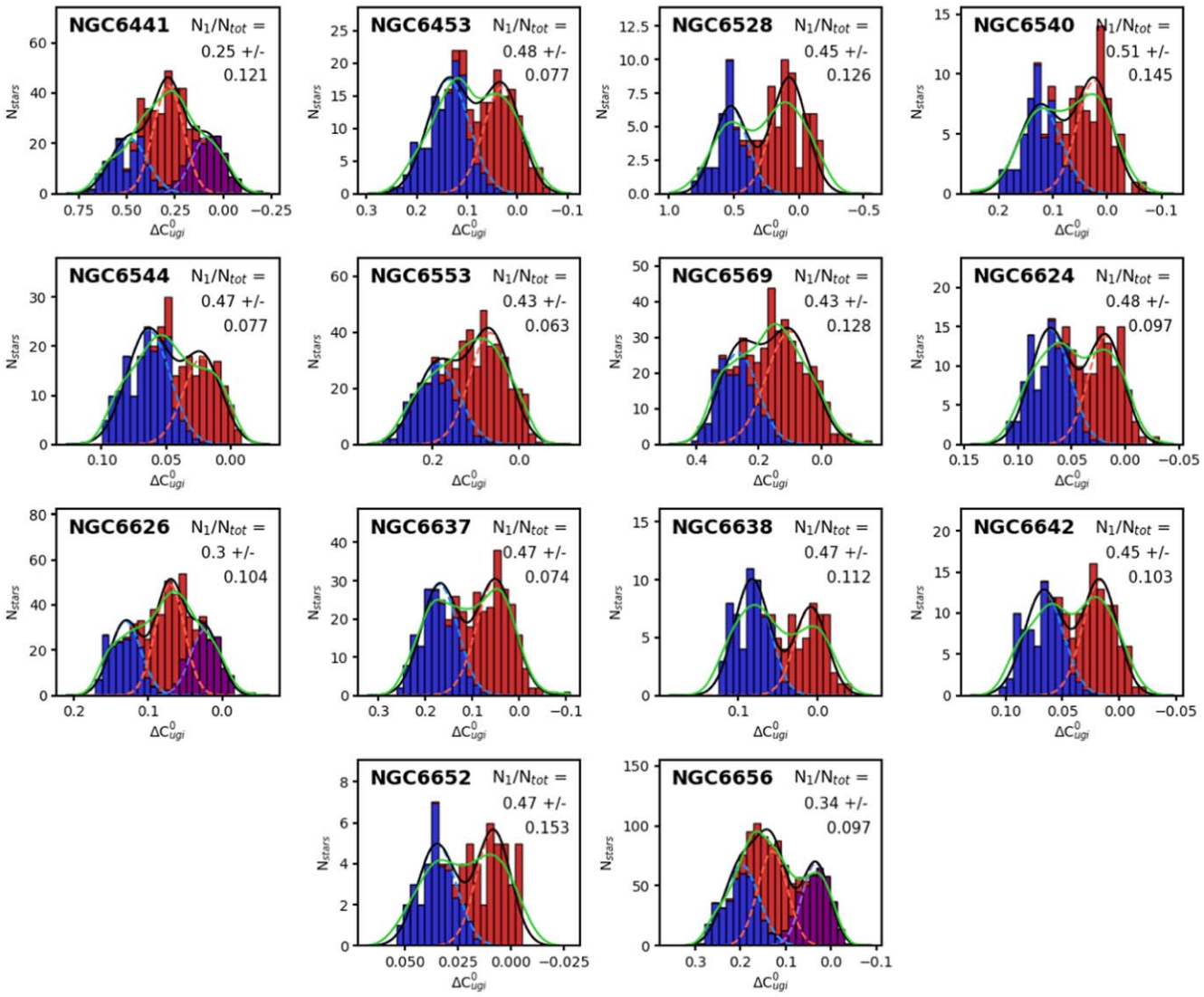

Figure 11. Pseudo-color offset (ΔC_{ugi}) distributions for the RGBs of each target bulge GC. The best-fitting Gaussian mixture models are represented as solid black curves. The individual model components are the dashed blue and red curves. Smoothed KDEs of the distributions are shown as green curves. The fraction of giant stars belonging to population 1 is related to the area under the blue Gaussian following the prescription described in Section 3.4.

NIR spectroscopic abundances from APOGEE are available for stars in several of our target clusters. In Figure 13, we show the Mg-Al diagrams for NGC 6553 and NGC 6656 from Mészáros et al. (2020), where we have adopted the use of [Al/Fe] = 0.3 as the demarcation line between 1G and 2G stars, as in that paper. In NGC 6544 (not shown) we were able to find spatial matches (1″) for four of the six APOGEE stars and compare their C_{ugi} colors to those of the RGB stars from BDBS. For this cluster, we do not find [Al/Fe]-selected 1G/2G stars to have distinct C_{ugi} colors. For NGC 6553 and NGC 6656, we spatially match BDBS with APOGEE using a 1″ radius and find that the Al-normal stars have blue C_{ugi} colors while the Al-enhanced stars have red C_{ugi} colors.

As a final point of comparison, we investigated whether the three populations identified in NGC 6441 could be validated using literature spectroscopic abundances. To this end, we collected Na and O abundances from Gratton et al. (2006, 2007) and APOGEE (Majewski et al. 2017). The comparisons are presented in Figure 14. In the left panel, we show the Na-O anticorrelation, which was divided visually into three groups: Group 1 (blue) are the Na-normal 1G stars, Group 2 (magenta) are the Na-enhanced 2G stars, and Group 3 are the *extreme* (Carretta et al. 2009) 2G stars with O-depleted atmospheres. The O-depleted stars that were matched to the BDBS catalog have preferentially red C_{ugi} colors. The mean C_{ugi} color of the Group 3 stars is consistent with the reddest peak in the RGB C_{ugi} color distribution of NGC 6441. The Group 1 stars have the bluest C_{ugi} colors, while the Group 2 stars have intermediate color. The median colors of Groups 1 and 2 are consistent with the 1P and 2P peaks of the C_{ugi} distribution to within 1σ and 2σ, respectively. We find three matching Group 1 stars, two from Gratton et al. (2006, 2007) and one from APOGEE (Majewski et al. 2017). The most Na-depleted star of these has a very blue C_{ugi} color. Overall, we find modest agreement between groups of stars tagged chemically versus photometrically with C_{ugi} in NGC 6441.

5. Discussion

5.1. Population Fraction–cluster Magnitude Correlation

In this section, we present a statistically significant anticorrelation ($r = 0.84 \pm 0.219$; $p < 0.001$) between the fraction of 1P stars and cluster absolute magnitude among our sample

Table 3
Derived Population Fractions for Each of the Sample Clusters, Along with an Estimate of the Total Uncertainty on the Result

Cluster	$(N_1/N_{\rm tot})_{10r_h}$ [a]	$(N_1/N_{\rm tot})_{1.6'}$ [b]	$(N_1/N_{\rm tot}^{\rm blue})$ [c]	$(N_1/N_{\rm tot})_{\rm M17}$ [c]
N6441	0.25 ± 0.121	0.25 ± 0.122	0.48 ± 0.157	⋯
N6453	0.48 ± 0.077	0.46 ± 0.082	⋯	⋯
N6528	0.45 ± 0.126	0.42 ± 0.131	⋯	⋯
N6540	0.51 ± 0.145	0.49 ± 0.175	⋯	⋯
N6544	0.47 ± 0.077	0.50 ± 0.075	⋯	⋯
N6553	0.43 ± 0.063	0.39 ± 0.061	⋯	⋯
N6569	0.43 ± 0.128	0.44 ± 0.135	⋯	⋯
N6624	0.48 ± 0.097	0.43 ± 0.071	⋯	0.279 ± 0.020
N6626	0.30 ± 0.104	0.30 ± 0.105	0.5 ± 0.151	⋯
N6637	0.47 ± 0.074	0.49 ± 0.078	⋯	0.425 ± 0.017
N6638	0.47 ± 0.112	0.47 ± 0.117	⋯	⋯
N6642	0.45 ± 0.103	0.47 ± 0.118	⋯	⋯
N6652	0.47 ± 0.153	0.44 ± 0.153	⋯	0.344 ± 0.026
N6656	0.34 ± 0.097	0.34 ± 0.097	0.48 ± 0.106	0.274 ± 0.020

Notes.
[a] Population fraction derived when including all stars out to $10r_{\rm h}$.
[b] Population fraction derived when including only stars inside $1\farcm6$ to match the HST/ACS field of view.
[c] Population fractions 1P/2P (bluest to intermediate, excluding the reddened component) for NGC 6441, NGC 6626, and NGC 6656.
[d] Population fraction derived in the HST study of M17, which covered a field of $\sim 1\farcm6$.

GCs. We place this result into context by comparing it with studies where population fractions were derived, and highlight differences pertaining to methodology and selection effects. We then discuss the connection between these two parameters in terms of cluster evolution. Additionally, we explore the mild correlation between 1P fraction and cluster metallicity.

Several sources in the literature comment on the correlation between the MP phenomenon and cluster mass: the spectroscopic study of Carretta et al. (2010b) results in a good correlation between IQR[Na/O] (a measure of the extent of the Na-O anticorrelation) and absolute V-band magnitude M_V; M17 report a strong correlation between the incidence of 1P stars and M_V; and Lagioia et al. (2019) find a strong correlation between RGB width in $C_{\rm F275W,F336W,F438W}$ and cluster mass. In particular, M17 find that their photometrically derived fraction of 1P stars is correlated significantly with M_V ($r = 0.72$; e.g., Figure 17). Many other studies compute population fractions (using either photometric tagging or spectroscopic abundances) but do not compare with cluster mass (Smolinski et al. 2011; Wang et al. 2016; Wang et al. 2017; Bowman et al. 2017; Lee 2019; Masseron et al. 2019). In Figure 15, we compare our derived 1P fractions (black symbols) with other literature studies, plotted against M_V. In the left panel, we color the points according to the study (see panel legend). The M17 results (gray) follow a similar trend line to our own; however, the other studies (which focus more on massive clusters) do not. On the other hand, when taken together, the literature results seem to generally corroborate with one another and indicate an anticorrelation (gray trend line in the right panel of Figure 15) between the 1P fraction and M_V in a fashion similar to our own results.

The literature comparisons are not precisely homogeneous, e.g., there is generally a mismatch in the radial extent of the stars studied in the clusters, and the population tagging followed different prescriptions. M17 uses HST WFC3/UVIS UV photometry from Piotto et al. (2015) to create chromosome maps of RGB stars in 44 mostly halo GCs. The space-based UV photometry easily splits the RGB stars into two clumps in the chromosome maps, and allowed the authors to compute 1P fractions for nearly all of the clusters in the sample. However, the small HST/WFC3 field of view restricted their study to the central parts of most of those clusters. Masseron et al. (2019) use APOGEE spectra of stars within 1 tidal radius of several northern GCs and use the spread in Al abundance as a measure of the extent of the MP phenomenon, and find a correlation with both metallicity and M_V. Meanwhile, Wang et al. (2016, 2017) use VLT/FLAMES to uncover population fractions based on Na abundance variations among RGB stars in several GCs. Bastian & Lardo (2015) use the Carretta et al. (2009) and Carretta et al. (2010b) spectroscopic data to derive population fractions and compare them with global cluster properties. Smolinski et al. (2011) count CN-normal and CN-enriched stars using Sloan Digital Sky Survey *ugriz* photometry of RGB stars within the tidal radius of eight GCs. Despite differences in methodology, the right panel of Figure 15 demonstrates a striking similarity between our results and a collection of literature results. The dispersion in the literature points is probably due in large part to differences in methodology and stellar sample selection.

The correlation between population fraction and cluster total M_V is not unexpected, indeed, cluster mass is thought to play a dominant role in determining the extent and complexity of the MP phenomenon in GCs (Carretta et al. 2010b; Bastian & Lardo 2018; Gratton et al. 2019; Nataf et al. 2019; Carretta 2019). The correlation between cluster mass, and, e.g., the fraction of 1P stars, is even more significant if initial cluster mass is considered instead of present cluster mass (Gratton et al. 2019). Baumgardt & Hilker (2018) derive masses and mass functions for the GCs studied in M17, and suggest that the correlation between the fraction of 1P stars and cluster mass is a result of more massive clusters being able to retain enriched gas from the 1P population, hence enabling the formation of more 2P stars than in less massive clusters. This picture is supported by the models of Vesperini et al. (2010) who find that the initial mass of the 2P population increases as a function of initial cluster mass, and by the models from Bekki et al. (2017), which indicate an increased loss of 1P AGB ejecta in lower mass clusters.

5.2. Comparison of Population Fraction with Other Cluster Properties

In terms of how other structural and environmental properties of GCs relate to the appearance of MPs, there is less agreement. For example, Gratton et al. (2019) interpret the correlation between the complexity of the chromosome maps of M17 with $R_{\rm apo}$ as evidence that massive clusters which formed farther out in the early Galaxy had a better chance of experiencing a more complex evolution than clusters that formed closer to the center. This picture is supported by Carretta et al. (2010b) who find that parameters related to the internal chemical evolution of the 19 clusters in their sample, e.g., $[{\rm O/Fe}]_{\rm min}$ and $[{\rm Na/Fe}]_{\rm max}$, are significantly correlated with some of the orbital properties of the clusters, including Galactocentric distance. The idea that the initial environment of the GC plays a role was further supported in Carretta (2019) where they replicated their study but on 95 GCs. On the other hand, Bastian & Lardo (2015), using the spectroscopic literature

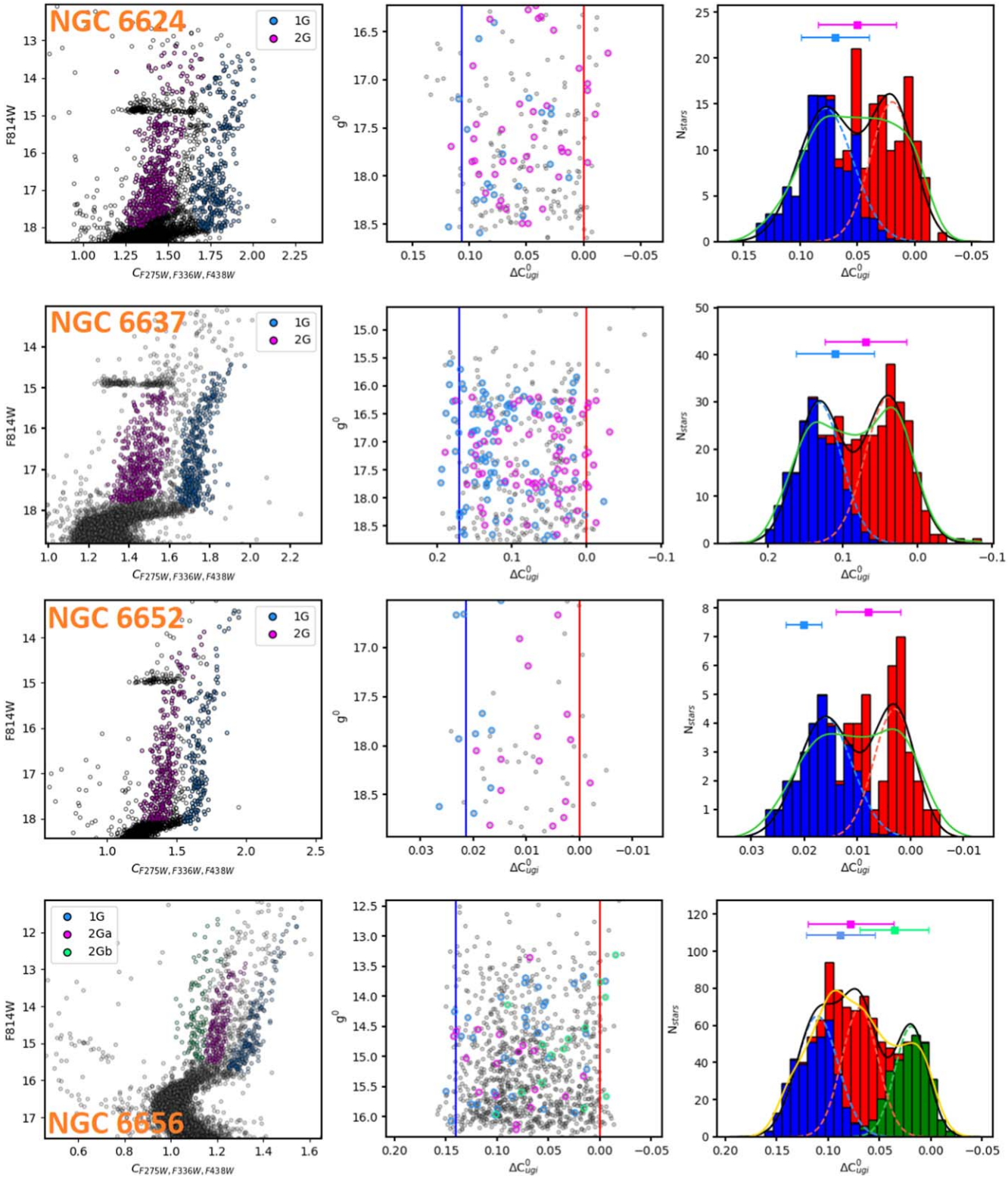

Figure 12. Comparison between populations derived using HST and BDBS photometry. The left panels show F814W vs. $C_{F275W,F336W,F438W}$ CMDs from Piotto et al. (2015), with hand-selected populations highlighted in cyan, magenta, and green. The center panels show the rectified BDBS RGBs in g vs. ΔC_{ugi}, with HST-matched stars colored according to their HST-selected population. The right panels show the ΔC_{ugi} distributions colored according to the GMM model, as in Figure 11. The mean (and standard deviation) of the ΔC_{ugi} colors of the matched HST 1G and 2G stars are shown as the cyan and magenta error bars. We find that stars forming separate sequences in the HST *magic trio* CMDs are also clearly segregated in ΔC_{ugi}.

results did not find any correlations between the fraction of 1P stars and Galactocentric distance. We do not find strong evidence for a correlation between the fraction of 1P stars and Galactocentric distance among our sample. However, because we are sampling a limited range in Galactocentric distance, and because that parameter alone does not dictate where the cluster spent much of its life (especially not for close-in bulge clusters, which could have migrated to their current positions, or may be

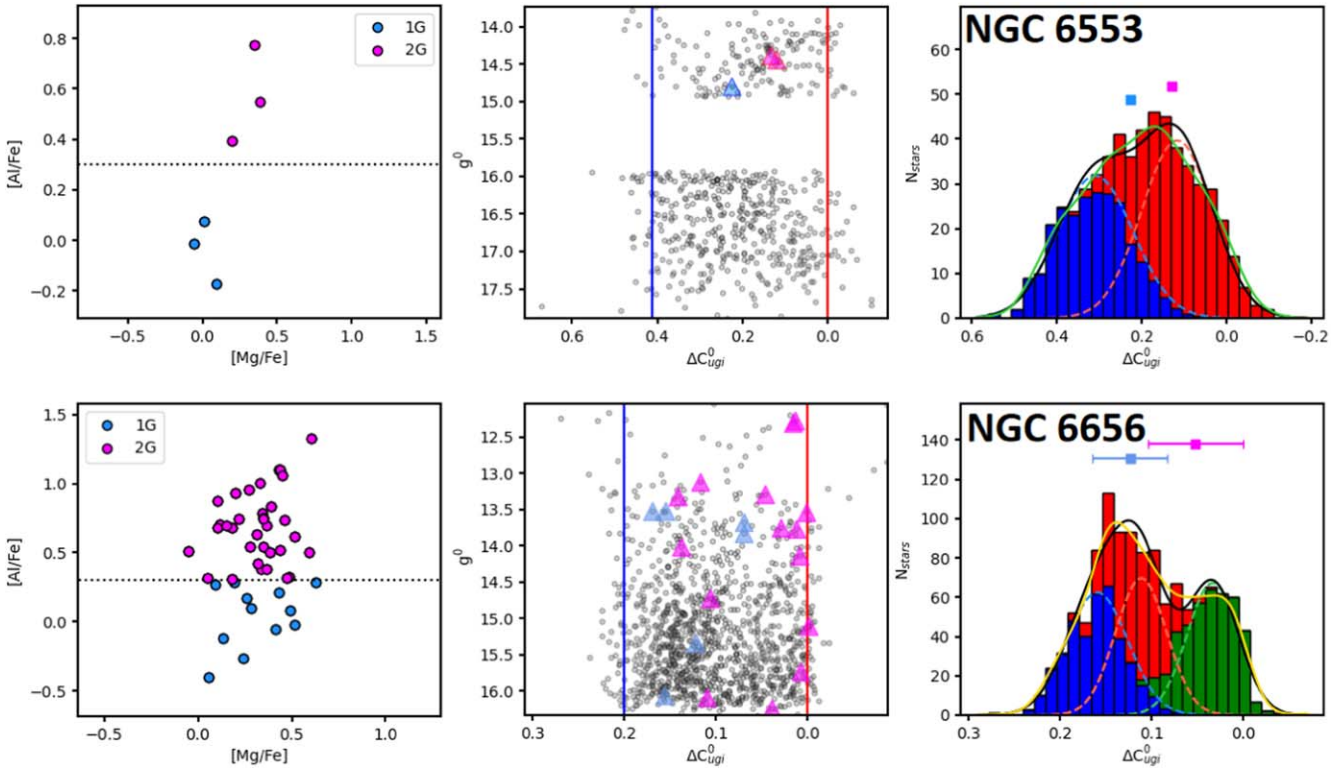

Figure 13. Comparison between BDBS photometrically selected populations and chemically selected groups using APOGEE spectroscopic abundances from the Mészáros et al. (2020). The left panels show Al vs. Mg abundances for RGB stars in each GC. Center panels show the rectified BDBS RGB (gray points) and stars crossmatched to the Mészáros et al. (2020) data set are color coded according to their Al abundance. As can be seen in the center and right-hand panels, Al-normal and Al-enhanced stars can be distinguished using C_{ugi}.

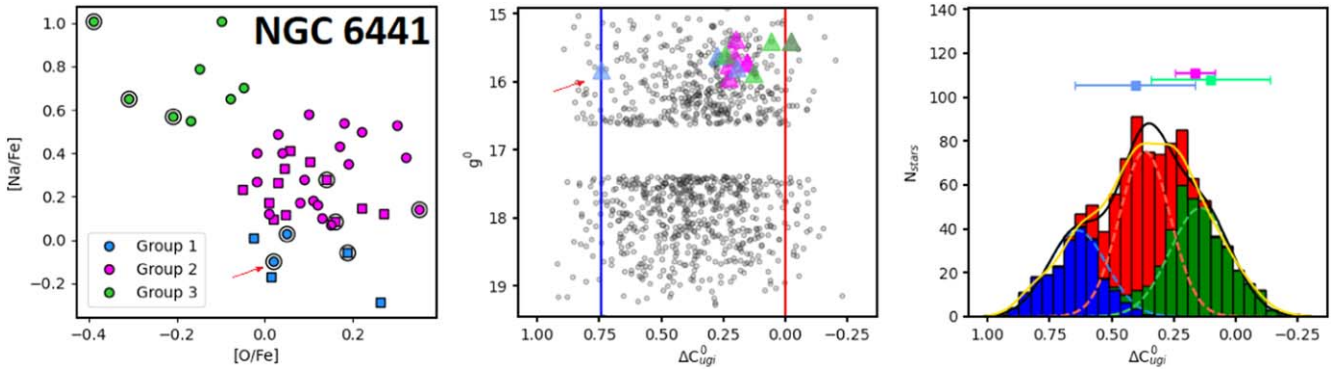

Figure 14. Comparison between spectroscopic abundances and populations identified using BDBS for NGC 6441. The abundances for NGC 6441 come from Gratton et al. (2006, 2007) and from APOGEE (Majewski et al. 2017), represented in the Na-O diagram as circles and squares, respectively. The left panel shows the Na-O anticorrelation, with hand-selected groups colored cyan, magenta, and green. The center panel is the BDBS rectified g vs. ΔC_{ugi} RGB. Stars with literature spectroscopic abundances were matched with BDBS spatially and are colored in the center panel according to their Na-O group. The matched stars are indicated with black circles in the Na-O diagram. The right panel shows the three-component GMM division of the ΔC_{ugi} distribution, along with the mean (and standard deviation) values of the ΔC_{ugi} colors for the three Na-O groups, which are shown as error bars above the histogram. There is modest agreement between the mean ΔC_{ugi} color of each Na-O group and the peaks of the main RGB populations determined using BDBS. We mark with a red arrow the star most depleted in Na from Gratton et al. (2007) (the APOGEE Na abundances had comparatively larger uncertainties). This star had a very blue C_{ugi} color.

bulge interlopers), we cannot rule out a relationship between the incidence of MPs and cluster environment.

We also investigated whether there might be a relationship between the fraction of 1P stars and [Fe/H]. As shown in the left panel of Figure 16, there is no correlation between literature $N_1/N_{\rm tot}$ values and [Fe/H], and we also find no significant correlation when using our own derived $N_1/N_{\rm tot}$ values. We also find no correlation between [Fe/H] and $N_1/N_{\rm tot}$ derived from a field limited to within 1.′6. However, when considering only the fraction of 1P stars in the blue RGBs of NGC 6441, NGC 6626, and NGC 6656 ($N_1/N^{\rm blue}_{\rm tot}$), i.e., excluding the reddest (potentially s-rich) component, we recover a mild correlation with [Fe/H], with a Pearson correlation coefficient of $r = -0.48 \pm 0.299$.

In the last decade, there have been contradicting results pertaining to whether, or how, metallicity plays a role in the formation and complexity of MPs. On the one hand, Bastian & Lardo (2015) compile a large body of literature on

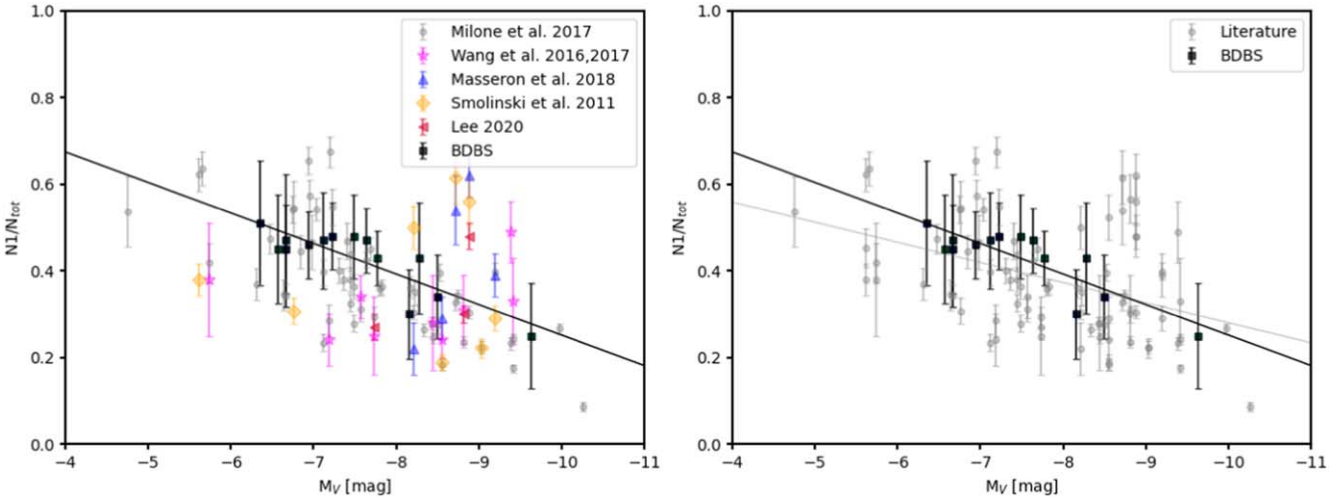

Figure 15. Derived population fraction $N_1/N_{\rm tot}$ vs. absolute cluster magnitude for the 14 clusters in this paper are denoted by black squares. In the left panel, we plot our results along with a selection of literature results. Individual studies do not tend to show the same trend as our results, except for the M17 results. This is likely due either to the small number of clusters in those studies, or to the limited cluster mass range of the studies. In the right panel, we plot the linear fit to the combined literature results (gray-filled circles), where it becomes evident that our result is consistent with the aggregate literature results. Our correlation has a Pearson rank correlation coefficient of $r = 0.84 \pm 0.219$ with a p-value of $p < 0.001$.

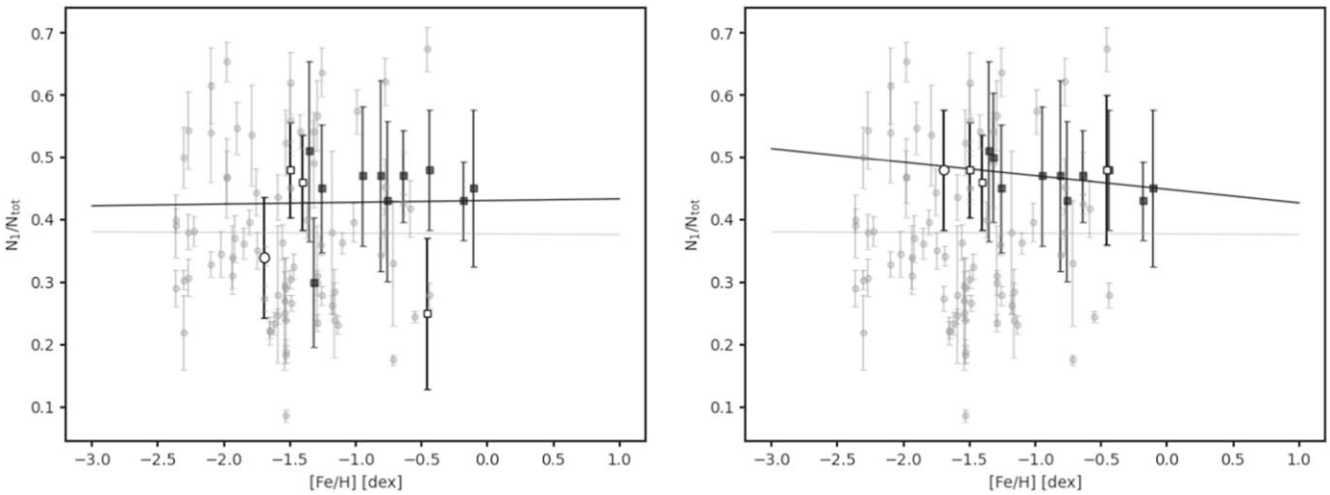

Figure 16. Both panels show the fraction of 1P stars as a function of cluster metallicity [Fe/H]. Black squares represent bulge GCs, white squares represent GCs currently passing through the inner Galaxy, and the white circle represents NGC 6656, which is a disk GC. Gray circles are a collection of GCs with population fractions drawn from the literature (the same as in Figure 15). In the right panel, we plot $N_1/N_{\rm tot}^{\rm blue}$ for NGC 6441, NGC 6626, and NGC 6656, i.e., 1P stars vs. intermediate population stars. We find a mild correlation ($r = -0.48 \pm 0.299$) between the fraction of 1P stars and cluster metallicity when we exclude the reddest, most enriched components of NGC 6441, NGC 6626, and NGC 6656. M17 find no significant correlation between these parameters ($r = -0.08 \pm 0.15$). Bastian & Lardo (2015) also find no correlation.

spectroscopic abundances and do not find any statistically significant trend between metallicity and the fraction of enriched stars, a finding that was further supported by M17 who also found that their derived fractions of 1P stars did not correlate with metallicity significantly ($r = -0.08$, $p = 0.6$). On the other hand, Smolinski et al. (2011) find a significant correlation between the fraction of 2P stars and cluster metallicity ($r = 0.78$); and while M17 did not find a correlation between population fraction and [Fe/H], they found a statistically significant correlation between the RGB width and [Fe/H] ($r = 0.79 \pm 0.05$). Meanwhile, Masseron et al. (2019) find a significant correlation ($r = -0.66$, $p = 0.038$) between the spread in Al and cluster metallicity for their 10 clusters, using APOGEE abundances. Since Al and Na abundances are correlated, this result suggests that there are fewer Na-rich (2P) stars as cluster metallicity increases, in contradiction to Smolinski et al. (2011) and M17 results. It would be interesting to expand our study to a larger number of bulge clusters, and to see whether we find a statistically significant trend of an increasing proportion of 1P stars with lower cluster metallicity, since consensus on the relation between population fraction and metallicity is critical in order to shed light on the nature of the 1P polluting stars (Gratton et al. 2012; Bastian & Lardo 2018; Gratton et al. 2019; Nataf et al. 2019).

5.3. Probing GC Populations Out to Large Radii

In this work, we have used photometry out to $10r_{\rm h}$ from the center of each cluster, farther than the studies done with HST. For most of the clusters, the $10r_{\rm h}$ selection accounts for stars out to, or nearly, one tidal radius, e.g., NGC 6441 ($0.7r_t$), NGC 6540 ($0.9r_t$), NGC 6637 ($1r_t$), NGC 6638 ($0.8r_t$), NGC 6642 (0.7), and NGC 6652 ($1r_t$). In some cases, we include extratidal

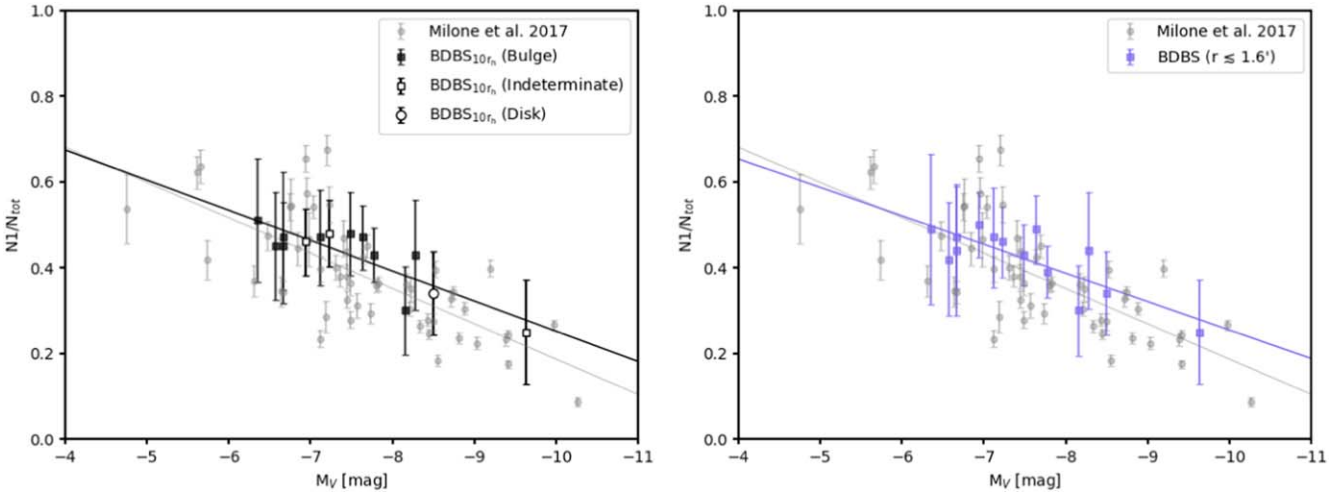

Figure 17. Derived population fraction vs. cluster absolute magnitude for the 14 clusters in the sample compared to the results from M17. The black symbols in the left panel are the results when including all stars within $10r_h$ of the cluster centers, and the pink symbols are the results when considering only stars within $2r_h$ of the cluster center, approximately matching the HST/WFC3 field. A vertical offset is not evident when comparing the full field (left panel) and the HST-matched inner field (right panel), i.e., the inner field appears to have a similar proportion of 1P stars. The right panel demonstrates that when we restrict our analysis to stars within the HST field, our results match well with the results from M17.

stars, e.g., for NGC 6544 ($5.9r_t$), NGC 6553 ($1.3r_t$), NGC 6626 ($1.7r_t$), and NGC 6656 ($1.2r_t$). For NGC 6453, NGC 6528, NGC 6569, and NGC 6624 we sample out to 0.2, 0.2, 0.4, and 0.4 r_t. We find that despite the differences in radial sampling, our derived population fractions are highly consistent with M17, as shown in the left panel of Figure 17, where our results are in striking accord with those from M17 both in terms of the cluster-to-cluster scatter and the slope of the trend line. When we restrict the analysis to stars within 1.′6 (Figure 17, right panel), the derived population fractions are still well correlated with M_V ($r = 0.8 \pm 0.233$), but do not become more consistent with the M17 trend line in a significant way. Smaller samples of stars and incompleteness of the Gaia-matched catalog within 1.′6 are likely the cause of increased scatter and error in $N_1/N_{\rm tot}$ for inner cluster stars in our study.

It is of interest whether clusters of the same mass have the same global population fraction. A complicating factor is the phenomenon of radial population gradients, which are a well-known feature in some GCs (Carretta et al. 2010a; Bastian & Lardo 2018). Unfortunately, the presence of radial population gradients may substantially bias measures of global population fraction: for a sample of clusters with equal mass, any existing radial population gradients will cause a scatter in $N_1/N_{\rm tot}$ if $r_{\rm max}/r_h$ is not the same for each cluster. In addition to consistency in choice of $r_{\rm max}/r_h$, it is also important to sample the clusters as completely as possible in order to separate any effect on $N_1/N_{\rm tot}$ caused by radial population gradients. Therefore, to understand how population fractions vary with cluster mass, it was critical to consistently include stars out to large-scale radii for all of the GCs in the sample.

6. Conclusions

In this work, we have used an unprecedented photometric data set to identify multiple stellar generations in the GCs of the southern Galactic bulge. We crossmatched our photometric data set with the Gaia EDR3 point-source catalog in order to select cluster members out to $10r_h$ based on PMs. Using the u, g, and i passbands, we utilized and tested the pseudo-color $(u-g)-(g-i)$ (C_{ugi}) as a probe for light element variations in cluster stars. We rectified the RGB of each GC to reveal multimodal or asymmetric C_{ugi} pseudo-color distributions, and used Gaussian mixture models to characterize the RGB subsequences. We presented this evidence to suggest the presence of multiple stellar populations in all of the brightest 14 globular clusters of the southern Galactic bulge, and derived the fraction of 1P (un-enriched) stars in each cluster. We found that the population ratios in these clusters correlate with cluster absolute visual magnitude and (mildly) with cluster metallicity. The correlation with M_V is statistically significant and matches well with previous studies. In conducting this study we are able to contribute metal-rich, inner galaxy GCs to the emerging picture of how multiple stellar populations relate to cluster properties and evolution. We have been able to use ground-based u-band photometry to build on and extend initial HST-based studies of multiple populations in globular clusters. In a forthcoming publication, we expand this analysis to include cluster candidate members beyond the tidal radius of the program clusters to study radial population trends and their correlation with cluster orbital and dynamical properties. This study demonstrates that ground-based u-band photometry as provided by DECam and eventually by the Vera C. Rubin Observatory, will prove powerful in the study of multiple populations in resolved globular clusters. Our main conclusions are:

1. BDBS photometry is useful for discriminating stellar populations using the pseudo-color index C_{ugi}.
2. We confirm the correlation between $N_1/N_{\rm tot}$ and M_V using BDBS photometry.
3. We extend the correlation to more metal-rich clusters.
4. By adding more metal-rich clusters, we find a marginally significant correlation with [Fe/H], but more clusters are needed to test this conclusion further.
5. We find that the proportion of 1P stars out to $10r_h$ and the 1P fraction for inner cluster stars both correlate significantly with M_V such that more massive clusters have a larger proportion of 2P stars.

The authors gratefully acknowledge financial support from the National Science Foundation under grants AST-1413755

and AST-1412673. A.J.K.H. gratefully acknowledges funding by the Deutsche Forschungsgemeinschaft (DFG, German Research Foundation)—Project-ID 138713538—SFB 881 ("The Milky Way System"), subprojects A03, A05, A11. A.M. K. acknowledges support from grant AST-2009836 from the National Science Foundation. C.I.J. gratefully acknowledges support from the HST Director's Discretionary Research Fund D0001.82494. Data used in this paper are from the Blanco DECam Survey Collaboration. This project used data obtained with the Dark Energy Camera (DECam), which was constructed by the Dark Energy Survey (DES) Collaboration. Funding for the DES Projects has been provided by the U.S. Department of Energy, the U.S. National Science Foundation, the Ministry of Science and Education of Spain, the Science and Technology Facilities Council of the United Kingdom, the Higher Education Funding Council for England, the National Center for Supercomputing Applications at the University of Illinois at Urbana-Champaign, the Kavli Institute of Cosmological Physics at the University of Chicago, the Center for Cosmology and Astro-Particle Physics at the Ohio State University, the Mitchell Institute for Fundamental Physics and Astronomy at Texas A&M University, Financiadora de Estudos e Projetos, Fundaçõ Carlos Chagas Filho de Amparo á Pesquisa do Estado do Rio de Janeiro, Conselho Nacional de Desenvolvimento Científico e Tecnológico and the Ministério da Ciência, Tecnologia e Inovacão, the Deutsche Forschungsgemeinschaft, and the Collaborating Institutions in the Dark Energy Survey. The Collaborating Institutions are Argonne National Laboratory, the University of California at Santa Cruz, the University of Cambridge, Centro de Investigaciones Enérgeticas, Medioambientales y Tecnológicas-Madrid, the University of Chicago, University College London, the DES-Brazil Consortium, the University of Edinburgh, the Eidgenössische Technische Hochschule (ETH) Zürich, Fermi National Accelerator Laboratory, the University of Illinois at Urbana-Champaign, the Institut de Cióncies de l'Espai (IEEC/CSIC), the Institut de Física dAltes Energies, Lawrence Berkeley National Laboratory, the Ludwig-Maximilians Universität München and the associated Excellence Cluster Universe, the University of Michigan, the National Optical Astronomy Observatory, the University of Nottingham, the Ohio State University, the OzDES Membership Consortium the University of Pennsylvania, the University of Portsmouth, SLAC National Accelerator Laboratory, Stanford University, the University of Sussex, and Texas A&M University. Based on observations at Cerro Tololo Inter-American Observatory (2013A-0529; 2014A-0480; PI: Rich), National Optical Astronomy Observatory, which is operated by the Association of Universities for Research in Astronomy (AURA) under a cooperative agreement with the National Science Foundation. This work has made use of data from the European Space Agency (ESA) mission Gaia (https://www.cosmos.esa.int/gaia), processed by the Gaia Data Processing and Analysis Consortium (DPAC, https://www.cosmos.esa.int/web/gaia/dpac/consortium). Funding for the DPAC has been provided by national institutions, in particular the institutions participating in the Gaia Multilateral Agreement. This research has made use of the SIMBAD database, operated at CDS, Strasbourg, France, as well as the VizieR catalog access tool, CDS (DOI:10.26093/cds/vizier). The original description of the VizieR service was published in 2000, A&AS 143, 23 This research has also made use of NASA's Astrophysics Data System Bibliographic Services. This work has made use of data from the European Space Agency (ESA) mission Gaia (https://www.cosmos.esa.int/gaia), processed by the Gaia Data Processing and Analysis Consortium (DPAC, https://www.cosmos.esa.int/web/gaia/dpac/consortium). Funding for the DPAC has been provided by national institutions, in particular the institutions participating in the Gaia Multilateral Agreement.

Appendix
PM Distributions and CMDs

Cluster member candidates were selected using Gaia EDR3 PMs, which were available for ∼40% of the BDBS stars in each cluster. We used Gaussian mixture models to distinguish between the distribution of cluster PMs and that of the Galactic field stars. We fit the one-dimensional $\mu_\alpha \cos(\delta)$ and μ_δ distributions separately. As a visual aid, we include the cluster mean $\mu_\alpha \cos(\delta)$ and μ_δ values from Vasiliev (2019) in the individual histograms (see Figures 18–21).

We tested GMMs with different numbers of components, and find that a nine-component model best captures the peak that is visually evident in the $\mu_\alpha \cos(\delta)$ and μ_δ distributions for all the clusters. Ultimately, we opted to choose stars within $r_{PM} \leqslant 1$ mas yr^{-1}, a value that was consistent with 2× the average standard deviation in $\mu_\alpha \cos(\delta)$ and μ_δ for most of the clusters. For NGC 6544 and NGC 6656, we selected stars within ∼3.3 and ∼3.7 mas yr^{-1} of the cluster mean value, respectively, since stars in these clusters had PM distributions significantly offset from those of the field.

In Figures 22–26, we summarize the selection of cluster stars for each GC in the sample. The left panels show 2D logarithmically scaled histograms of stellar surface number density as a function of position for all BDBS stars within $10r_{\rm h}$ of each cluster. The center panels show the PM distribution for all stars within $10r_{\rm h}$: the location of the cluster median value is marked as a red cross, and the selection region is shown as a black circle. Stars with PMs inside the black circle are colored black in the left and right panels. The right panels show the differential reddening-corrected r versus $u - r$ CMDs, for all stars inside $10r_{\rm h}$ (2D histogram), and for the stars with cluster-like PMs (black dots). Each cluster has an easily identifiable RGB. Uncertainty on C_{ugi} colors, which are the u, g, and i apparent magnitude errors added in quadrature, are computed as a function of r magnitude and are represented as error bars in the right panels.

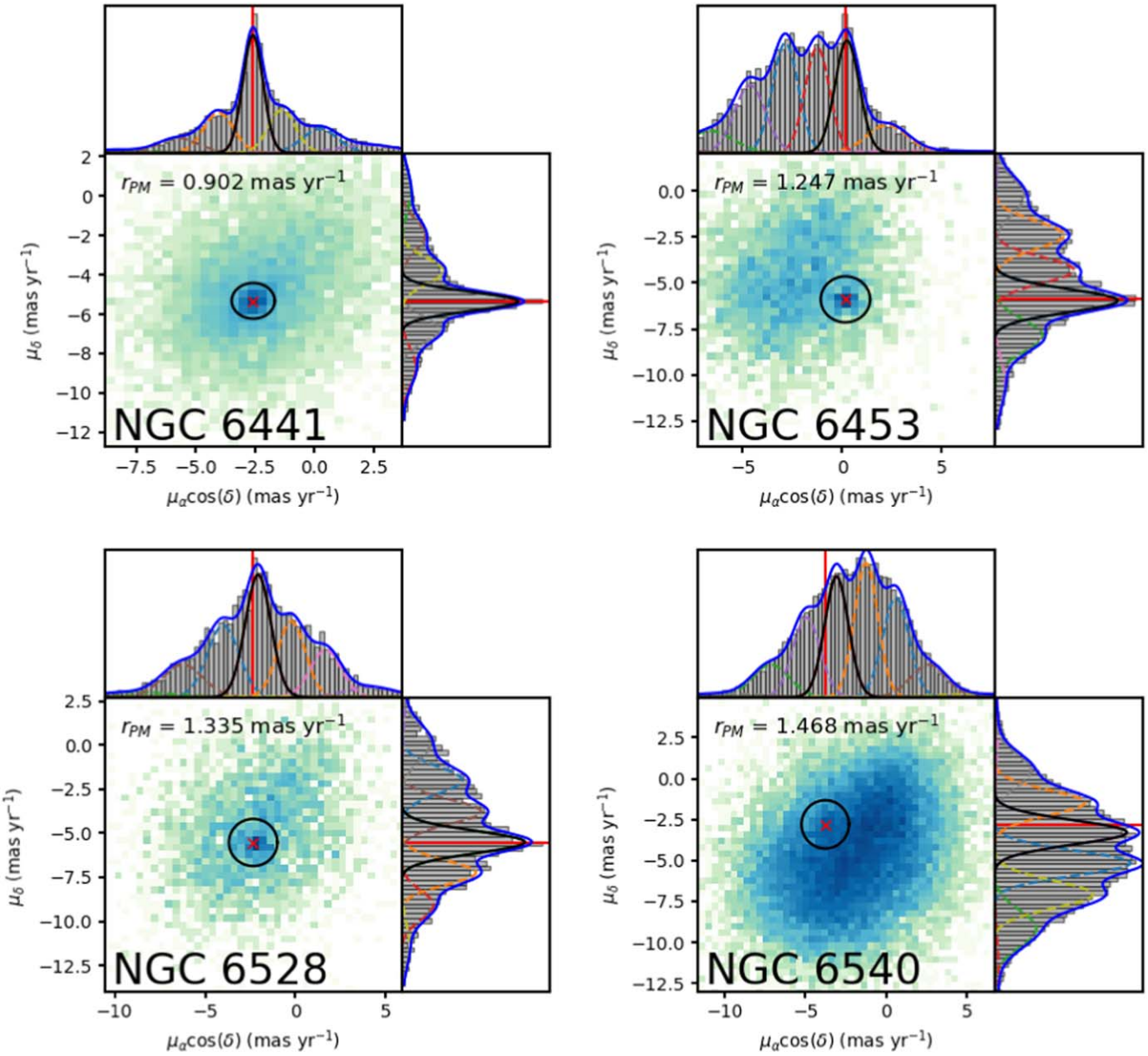

Figure 18. Summary of the PM selection for NGC 6441, NGC 6453, NGC 6528, and NGC 6540. The 2D distribution of PMs for all stars within 10 $r_{\rm h}$ of the cluster center is shown in the main panel, centered on the mean PM of the cluster itself from Vasiliev (2019), marked with a red cross in each case. Above and to the right of the main panels are the distributions in $\mu_\alpha \cos(\delta)$ and μ_δ, respectively. The distributions are fit with nine-component GMMs, where the sum of the components is shown as a blue line. The cluster $\mu_\alpha \cos(\delta)$ and μ_δ distributions are modeled as the bold black Gaussian components, which were identified as those with centroids most consistent with the cluster mean PMs (indicated with red lines in the histograms). We label for each cluster $r_{\rm PM}$, which is 2× the mean of the σ values of the cluster $\mu_\alpha \cos(\delta)$ and μ_δ distributions. The black circles have a radius $r = r_{\rm PM}$.

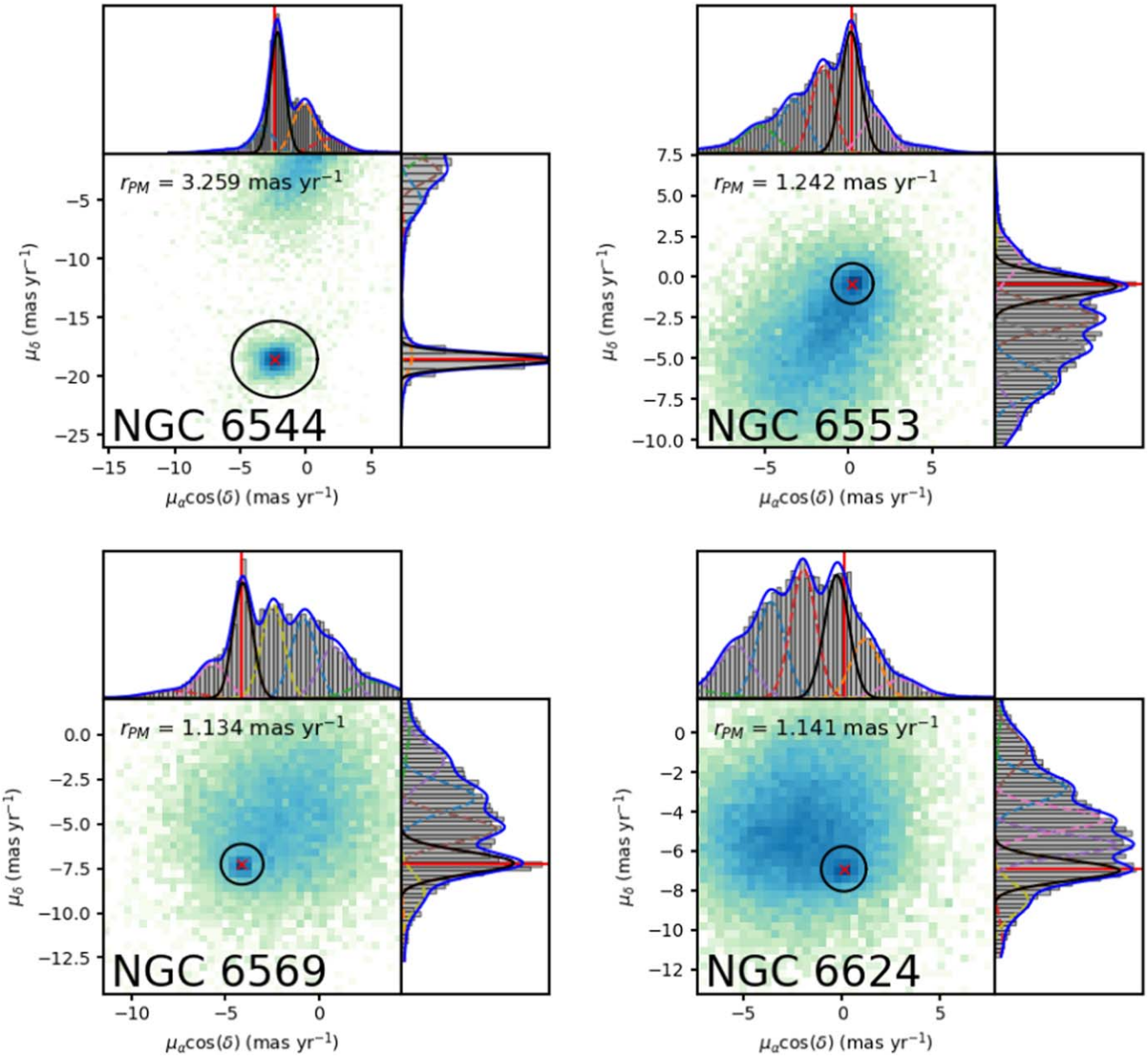

Figure 19. Same as Figure 18, but for NGC 6544, NGC 6553, NGC 6569, and NGC 6624. Note the clear separation of the NGC 6544 cluster PM distribution from the PM distribution of the field stars.

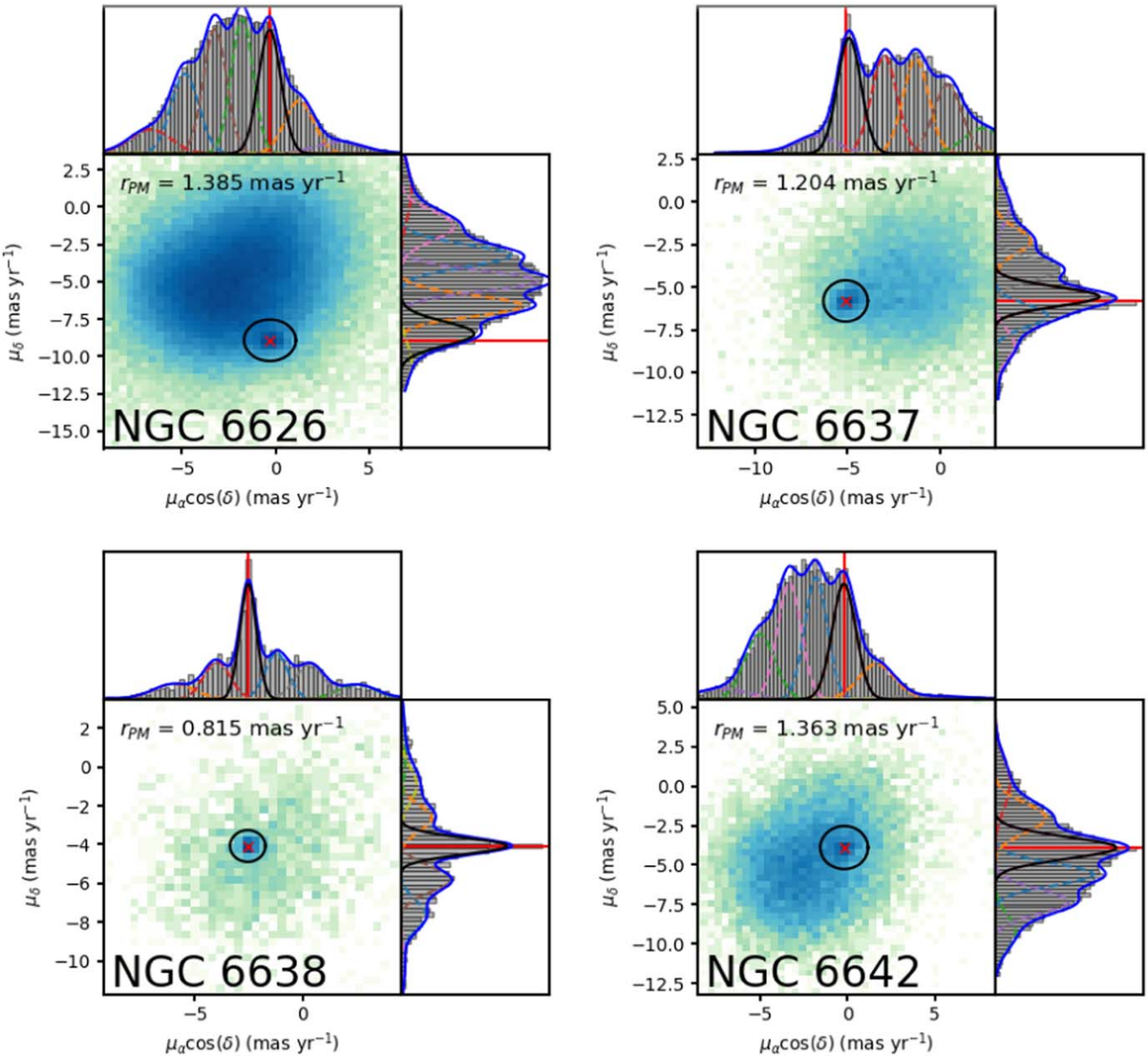

Figure 20. Same as Figure 18, but for NGC 6626, NGC 6637, NGC 6638, and NGC 6642.

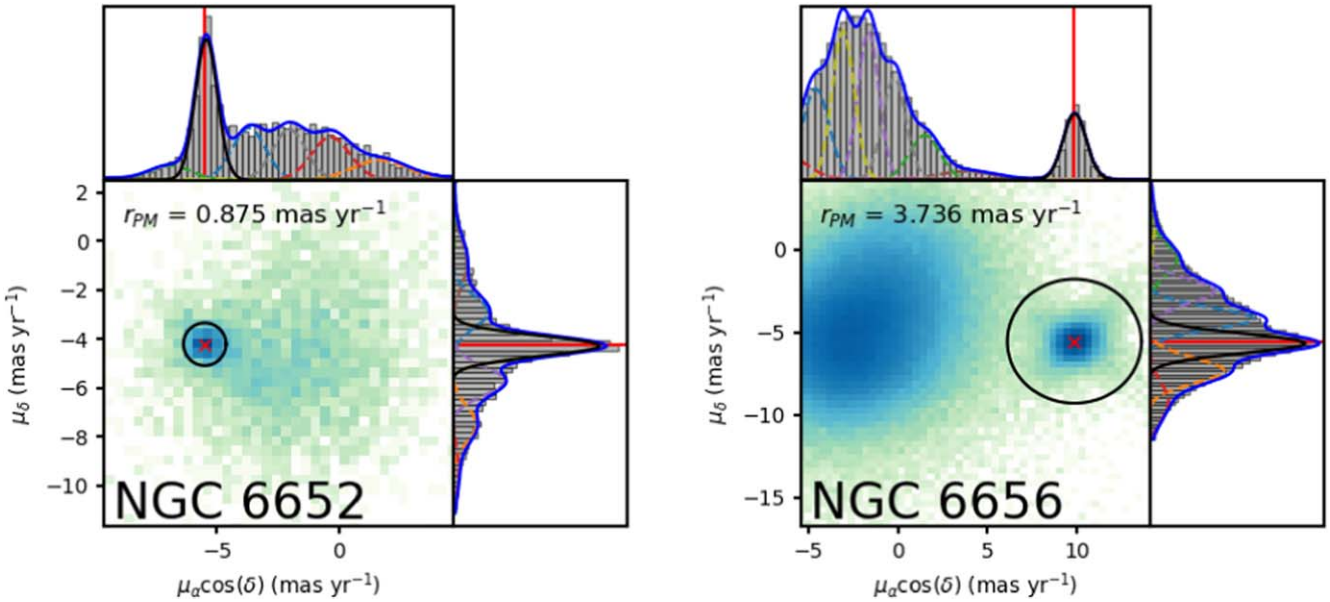

Figure 21. Same as Figure 18, but for NGC 6652 and NGC 6656. The PM distribution of NGC 6656 is clearly defined with respect to the PM distribution of the field stars, and the selection region was set at the 6σ level of the normal distribution used to model it.

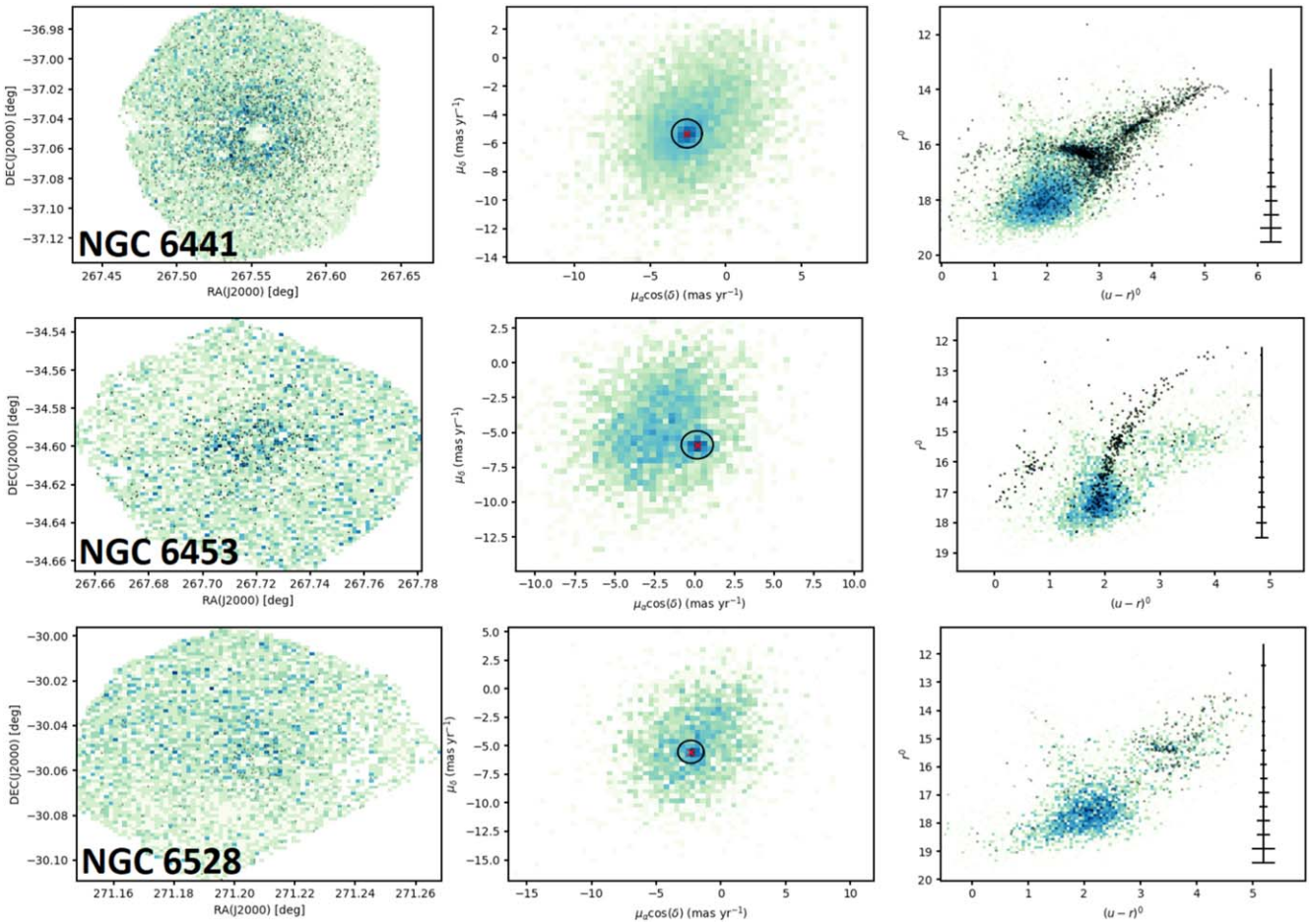

Figure 22. Summary panels for the selection of cluster stars for NGC 6441, NGC 6453, and NGC 6528. Left panels show the 2D histogram of the logarithm of the surface number density of all BDBS stars within $10r_h$ from the cluster center. The center panels show 2D histograms of the PM distribution of all Gaia-matched BDBS stars within $10r_h$ of the cluster center, which is marked as a red cross. The right panels show the differential reddening-corrected CMD of all stars BDBS stars inside $10r_h$ of the cluster center as a 2D histogram. Black stars in the CMDs (and in the left panels) are stars that have PMs consistent with cluster membership (inside the black circles in the center panels). The RGBs of each of the three clusters are identifiable. Photometric measurement errors as a function of r magnitude are shown in the right panels.

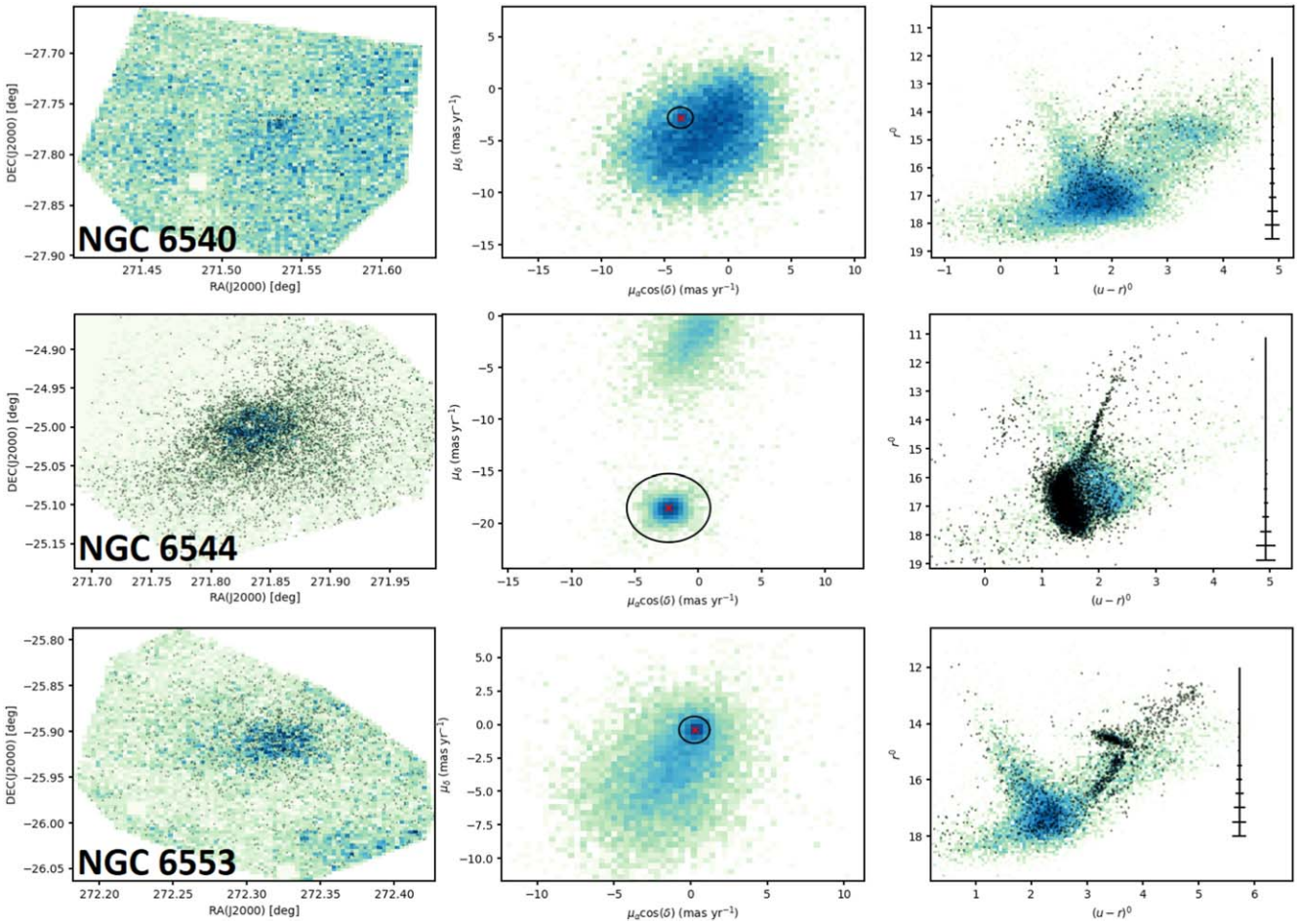

Figure 23. Same as Figure 22, but for NGC 6540, NGC 6544, and NGC 6553. NGC 6540 was particularly difficult to separate from the field, since the local density of field stars is very high and since the cluster does not have PMs offset significantly from the field. We chose a PM selection radius of 0.5 mas yr^{-1} for this cluster. For NGC 6544, the situation is reversed because the cluster PMs are clearly distinguished from the field, so we chose a PM selection radius of 3.3 mas yr^{-1}. All three clusters have a readily identifiable RGB.

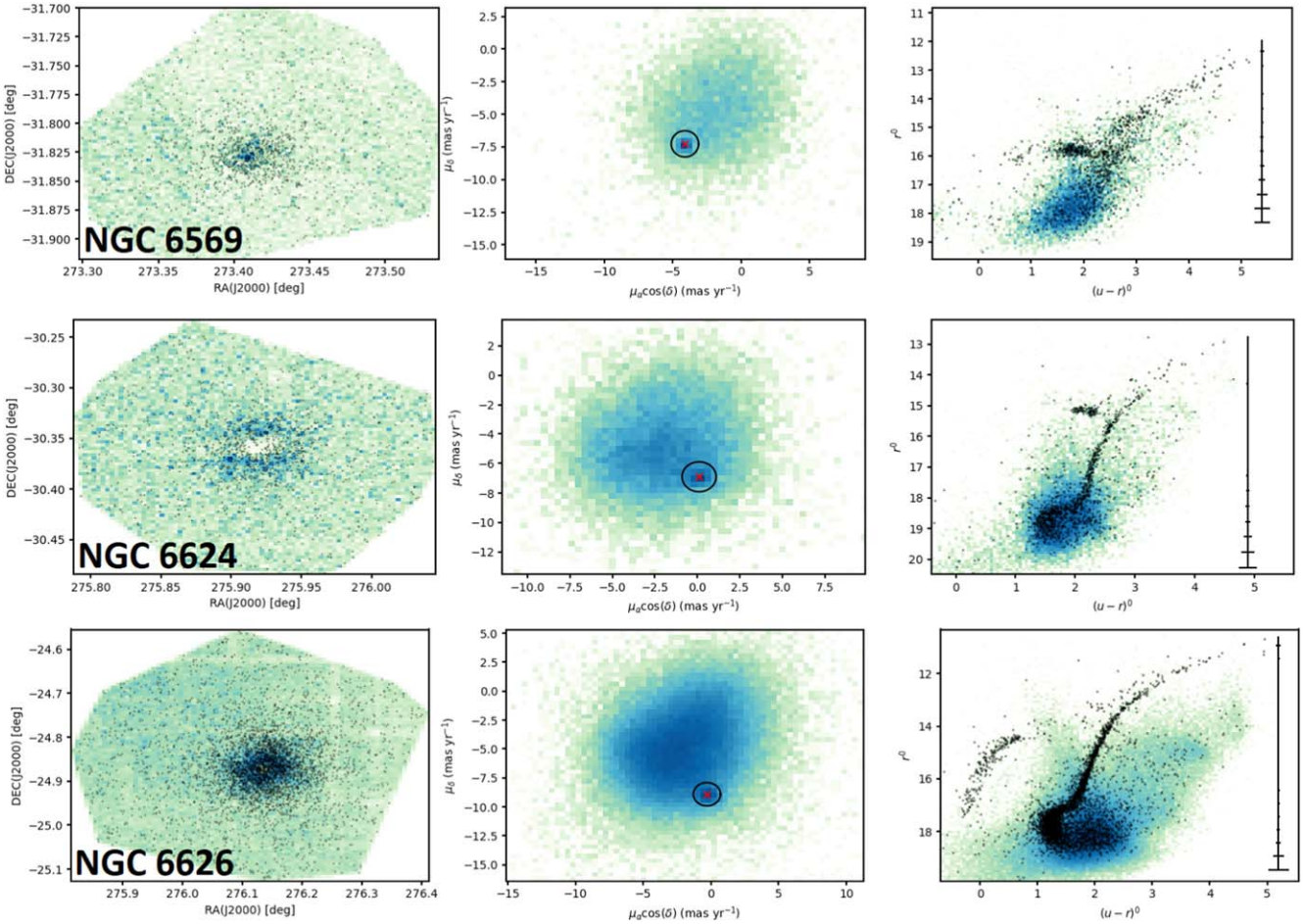

Figure 24. Same as Figure 22, but for NGC 6569, NGC 6624, and NGC 6626.

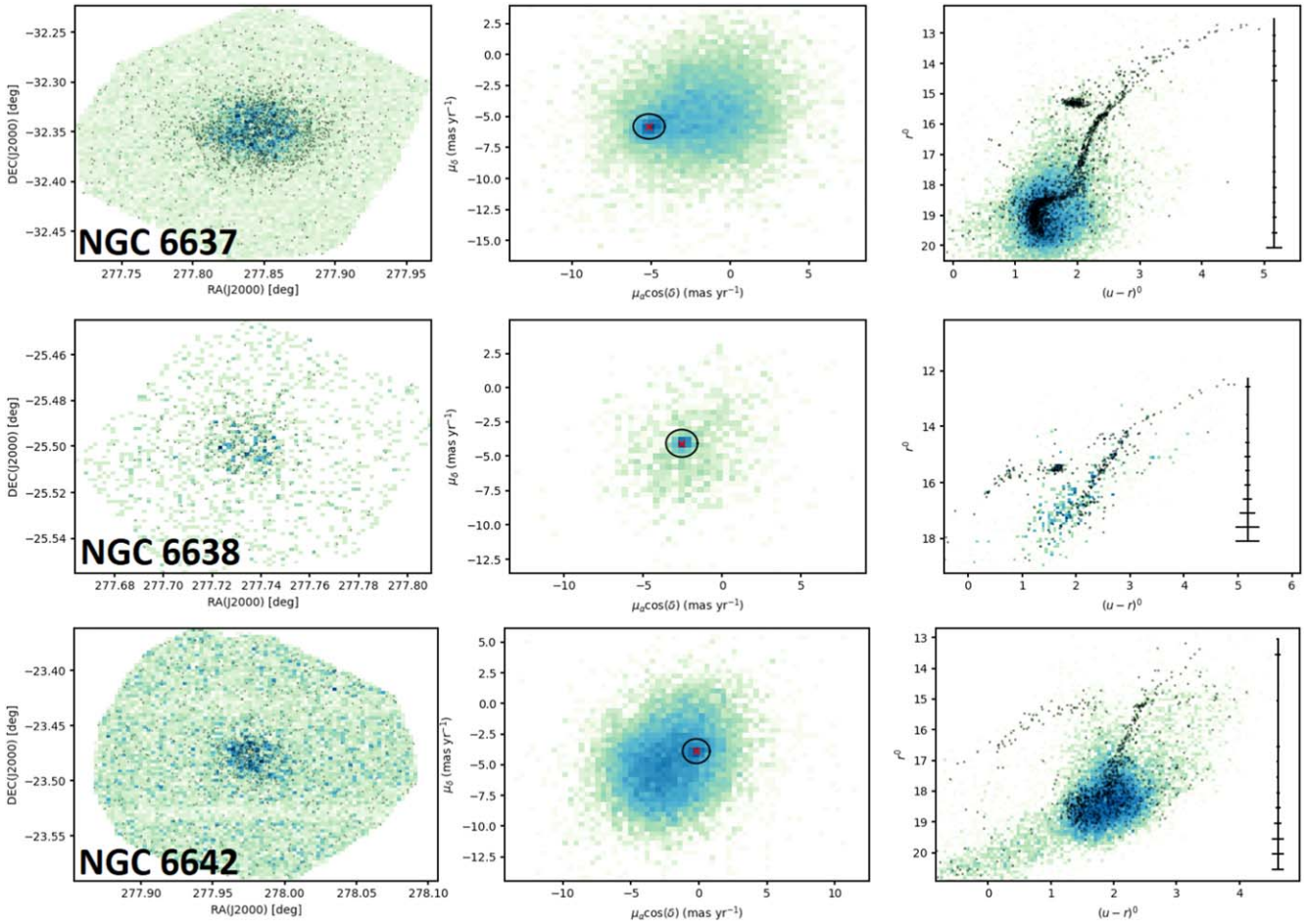

Figure 25. Same as Figure 22, but for NGC 6637, NGC 6638, and NGC 6642.

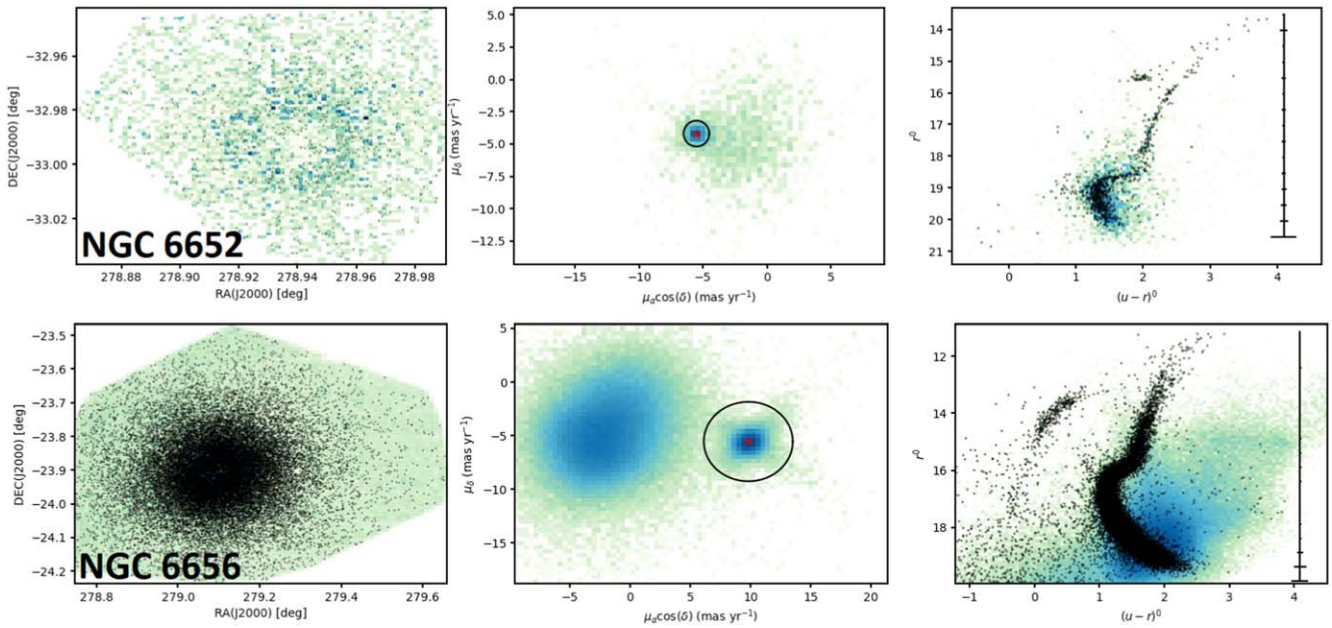

Figure 26. Same as Figure 22, but for NGC 6652 and NGC 6656. Note that NGC 6656 has a PM distribution offset from the field star PM distribution, so a correspondingly large PM selection radius of 3.7 mas yr^{-1} was chosen.

ORCID iDs

Justin A. Kader https://orcid.org/0000-0002-6650-3757
Catherine A. Pilachowski https://orcid.org/0000-0002-3007-206X
Christian I. Johnson https://orcid.org/0000-0002-8878-3315
R. Michael Rich https://orcid.org/0000-0003-0427-8387
Michael D. Young https://orcid.org/0000-0002-0036-941X
Iulia T. Simion https://orcid.org/0000-0001-8889-0762
William I. Clarkson https://orcid.org/0000-0002-2577-8885
Scott Michael https://orcid.org/0000-0002-0509-1197
Andrea Kunder https://orcid.org/0000-0002-2808-1370
Anna Katherina Vivas https://orcid.org/0000-0003-4341-6172
Andreas J. Koch-Hansen https://orcid.org/0000-0002-9859-4956
Tommaso Marchetti https://orcid.org/0000-0003-0064-0692

References

Barbuy, B., Bica, E., & Ortolani, S. 1998, A&A, 333, 117
Bastian, N., & Lardo, C. 2015, MNRAS, 453, 357
Bastian, N., & Lardo, C. 2018, ARA&A, 56, 83
Baumgardt, H., & Hilker, M. 2018, MNRAS, 478, 1520
Baumgardt, H., Sollima, A., & Hilker, M. 2020, PASA, 37, e046
Bekki, K., Jeřábková, T., & Kroupa, P. 2017, MNRAS, 471, 2242
Bellini, A., Piotto, G., Milone, A. P., et al. 2013, ApJ, 765, 32
Bica, E., Ortolani, S., & Barbuy, B. 2016, PASA, 33, e028
Boberg, O. M., Friel, E. D., & Vesperini, E. 2015, ApJ, 804, 109
Bonatto, C., Chies-Santos, A. L., Coelho, P. R. T., et al. 2019, A&A, 622, A179
Bono, G., Dall'Ora, M., Fabrizio, M., et al. 2018, arXiv:1812.03124
Bowman, W. P., Pilachowski, C. A., van Zee, L., et al. 2017, AJ, 154, 131
Buitinck, L., Louppe, G., Blondel, M., et al. 2013, arXiv:1309.0238
Busso, G., Cassisi, S., Piotto, G., et al. 2007, A&A, 474, 105
Caloi, V., & D'Antona, F. 2007, A&A, 463, 949
Carretta, E. 2019, A&A, 624, A24
Carretta, E., Bragaglia, A., D'Orazi, V., et al. 2010a, A&A, 519, A71
Carretta, E., Bragaglia, A., Gratton, R. G., et al. 2009, A&A, 505, 117
Carretta, E., Bragaglia, A., Gratton, R. G., et al. 2010b, A&A, 516, A55
Carretta, E., Bragaglia, A., Gratton, R. G., et al. 2014, A&A, 561, A87
Cohen, J. G. 1978, ApJ, 223, 487
Colucci, J. E., Bernstein, R. A., & Cohen, J. G. 2014, ApJ, 797, 116
Côté, P. 1999, AJ, 118, 406
D'Ercole, A., Vesperini, E., D'Antona, F., McMillan, S. L. W., & Recchi, S. 2008, MNAS, 391, 825
di Criscienzo, M., Ventura, P., D'Antona, F., et al. 2010, MNRAS, 408, 999
Dias, B., Barbuy, B., Saviane, I., et al. 2016, A&A, 590, A9
Ferraro, F. R., Dalessandro, E., Mucciarelli, A., et al. 2009, Natur, 462, 483
Ferraro, F. R., Pallanca, C., Lanzoni, B., et al. 2021, NatAs, 5, 311
Frenk, C. S., & White, S. D. M. 1982, MNRAS, 198, 173
Gaia Collaboration, Brown, A. G. A., Vallenari, A., et al. 2021, A&A, 649, A1
Gaia Collaboration, Helmi, A., van Leeuwen, F., et al. 2018, A&A, 616, A12
Geisler, D., Villanova, S., O'Connell, J. E., et al. 2021, A&A, 652, A157
Gerber, J. M., Briley, M. M., & Smith, G. H. 2019, AJ, 157, 154
Gratton, R. G., Bonifacio, P., Bragaglia, A., et al. 2001, A&A, 369, 87
Gratton, R., Bragaglia, A., Carretta, E., et al. 2019, A&ARv, 27, 8
Gratton, R. G., Carretta, E., & Bragaglia, A. 2012, A&ARv, 20, 50
Gratton, R. G., Lucatello, S., Bragaglia, A., et al. 2006, A&A, 455, 271
Gratton, R. G., Lucatello, S., Bragaglia, A., et al. 2007, A&A, 464, 953
Harding, G. A. 1962, Obs, 82, 205
Harris, W. E. 1996, AJ, 112, 1487
Hartmann, E. A., Bonatto, C. J., Chies-Santos, A. L., et al. 2022, MNRAS, 515, 4191
Hollyhead, K., Kacharov, N., Lardo, C., et al. 2017, MNRAS, 465, L39
Johnson, C. I., Rich, R. M., Young, M. D., et al. 2020, MNRAS, 499, 2357
Kader, J., Pilachowski, C., Johnson, C., et al. 2022, ApJ, submitted
Kerber, L. O., Nardiello, D., Ortolani, S., et al. 2018, ApJ, 853, 15
Lagioia, E. P., Milone, A. P., Marino, A. F., et al. 2019, AJ, 158, 202
Lardo, C., Bellazzini, M., Pancino, E., et al. 2011, A&A, 525, A114
Larsen, S. S., Brodie, J. P., Forbes, D. A., et al. 2014, A&A, 565, A98
Lee, J.-W. 2015, ApJS, 219, 7
Lee, J.-W. 2019, ApJ, 872, 41
Lee, J.-W. 2020, ApJL, 888, L6
Letarte, B., Hill, V., Jablonka, P., et al. 2006, A&A, 453, 547
Lim, D., Koch-Hansen, A. J., Chung, C., et al. 2021, A&A, 647, A34
Majewski, S. R., Schiavon, R. P., Frinchaboy, P. M., et al. 2017, AJ, 154, 94
Marchetti, T., Johnson, C. I., Joyce, M., et al. 2022, A&A, 664, A124
Marino, A. F., Milone, A. P., Piotto, G., et al. 2009, A&A, 505, 1099
Marino, A. F., Milone, A. P., Sneden, C., et al. 2012, A&A, 541, A15
Marino, A. F., Sneden, C., Kraft, R. P., et al. 2011, A&A, 532, A8
Marino, A. F., Villanova, S., Piotto, G., et al. 2008, A&A, 490, 625
Massari, D., Koppelman, H. H., & Helmi, A. 2019, A&A, 630, L4
Massari, D., Mucciarelli, A., Ferraro, F. R., et al. 2014, ApJ, 791, 101
Masseron, T., García-Hernández, D. A., Mészáros, S., et al. 2019, A&A, 622, A191
Mészáros, S., Masseron, T., García-Hernández, D. A., et al. 2020, MNRAS, 492, 1641
Mauro, F., Moni Bidin, C., Geisler, D., et al. 2014, A&A, 563, A76
Milone, A. P., Piotto, G., Renzini, A., et al. 2017, MNRAS, 464, 3636
Minniti, D. 1995, AJ, 109, 1663
Minniti, D., Lucas, P. W., Emerson, J. P., et al. 2010, NewA, 15, 433
Monelli, M., Milone, A. P., Stetson, P. B., et al. 2013, MNRAS, 431, 2126
Moni Bidin, C., Mauro, F., Contreras Ramos, R., et al. 2021, A&A, 648, A18
Mucciarelli, A., Carretta, E., Origlia, L., et al. 2008, AJ, 136, 375
Mucciarelli, A., Lapenna, E., Massari, D., et al. 2015, ApJ, 809, 128
Mucciarelli, A., Origlia, L., Ferraro, F. R., et al. 2009, ApJL, 695, L134
Mucciarelli, A., Origlia, L., & Ferraro, F. R. 2010, ApJ, 717, 277
Muñoz, C., Villanova, S., Geisler, D., et al. 2020, MNRAS, 492, 3742
Nataf, D. M., Wyse, R. F. G., Schiavon, R. P., et al. 2019, AJ, 158, 14
Origlia, L., Massari, D., Rich, R. M., et al. 2013, ApJL, 779, L5
Ortolani, S., Renzini, A., Gilmozzi, R., et al. 1995, Natur, 377, 701
Piatti, A. E., & Koch, A. 2018, ApJ, 867, 8
Piotto, G. 2008, MmSAI, 79, 334
Piotto, G., Bedin, L. R., Anderson, J., et al. 2007, ApJL, 661, L53
Piotto, G., Milone, A. P., Bedin, L. R., et al. 2015, AJ, 149, 91
Pérez-Villegas, A., Barbuy, B., Kerber, L. O., et al. 2020, MNRAS, 491, 3251
Popper, D. M. 1947, ApJ, 105, 204
Renzini, A. 2008, MNRAS, 391, 354
Rich, R. M., Johnson, C. I., Young, M., et al. 2020, MNRAS, 499, 2340
Rossi, L. J., Ortolani, S., Barbuy, B., et al. 2015, MNRAS, 450, 3270
Sakari, C. M., Venn, K. A., Mackey, D., et al. 2015, MNRAS, 448, 1314
Salinas, R., & Strader, J. 2015, ApJ, 809, 169
Saracino, S., Dalessandro, E., Ferraro, F. R., et al. 2015, ApJ, 806, 152
Sbordone, L., Monaco, L., Moni Bidin, C., et al. 2015, A&A, 579, A104
Sbordone, L., Salaris, M., Weiss, A., et al. 2011, A&A, 534, A9
Schiavon, R. P., Caldwell, N., Conroy, C., et al. 2013, ApJL, 776, L7
Schiavon, R. P., Johnson, J. A., Frinchaboy, P. M., et al. 2017a, MNRAS, 466, 1010
Schiavon, R. P., Zamora, O., Carrera, R., et al. 2017b, MNRAS, 465, 501
Scott, D. W. 1979, Biometrika, 66, 605
Simion, I. T., Belokurov, V., Irwin, M., et al. 2017, MNRAS, 471, 4323
Smolinski, J. P., Martell, S. L., Beers, T. C., et al. 2011, AJ, 142, 126
Tang, B., Cohen, R. E., Geisler, D., et al. 2017, MNRAS, 465, 19
Tang, B., Fernández-Trincado, J. G., Liu, C., et al. 2020, ApJ, 891, 28
Valcarce, A. A. R., & Catelan, M. 2011, A&A, 533, A120
Vasiliev, E. 2019, MNRAS, 484, 2832
Vesperini, E., Hong, J., Giersz, M., et al. 2021, MNRAS, 502, 4290
Vesperini, E., McMillan, S. L. W., D'Antona, F., et al. 2010, ApJL, 718, L112
Villanova, S., Moni Bidin, C., Mauro, F., et al. 2017, MNRAS, 464, 2730
Wagner-Kaiser, R., Stenning, D. C., Sarajedini, A., et al. 2016, MNRAS, 463, 3768
Wang, Y., Primas, F., Charbonnel, C., et al. 2016, A&A, 592, A66
Wang, Y., Primas, F., Charbonnel, C., et al. 2017, A&A, 607, A135
Yong, D., Grundahl, F., Johnson, J. A., et al. 2008, ApJ, 684, 1159
Yoon, S.-J., Joo, S.-J., Ree, C. H., et al. 2008, ApJ, 677, 1080
Zinn, R. 1996, in ASP Conf. Ser. 92, Formation of the Galactic Halo... Inside and Out, ed. H. Morrison & A. Sarajedini (San Francisco, CA: ASP), 211